Journal of Structural Geology 32 (2010) 900–919

Contents lists available at ScienceDirect

Journal of Structural Geology

journal homepage: www.elsevier.com/locate/jsg

Kinematic evolution of the Ama Drime detachment: Insights into orogen-parallel extension and exhumation of the Ama Drime Massif, Tibet–Nepal

Jackie M. Langille [a,*], Micah J. Jessup [a], John M. Cottle [b], Dennis Newell [c], Gareth Seward [b]

[a] Department of Earth and Planetary Sciences, University of Tennessee, Knoxville, TN 37996, USA
[b] Department of Earth Science, University of California, Santa Barbara, CA 93106, USA
[c] Earth and Environmental Sciences, Los Alamos National Laboratory, Los Alamos, NM 87545, USA

ARTICLE INFO

Article history:
Received 13 June 2009
Received in revised form
25 March 2010
Accepted 11 April 2010
Available online 20 April 2010

Keywords:
Himalaya
Microstructures
Vorticity techniques
Quartz fabrics
Two-feldspar geothermometry
Detachment dynamics

ABSTRACT

The Ama Drime Massif is a north–south trending antiformal structure located on the southern margin of the Tibetan Plateau that is bound by the Ama Drime and Nyönno Ri detachments on the western and eastern sides, respectively. Detailed kinematic and vorticity analyses were combined with deformation temperature estimates on rocks from the Ama Drime detachment to document spatial and temporal patterns of deformation. Deformation temperatures estimated from quartz and feldspar microstructures, quartz [*c*] axis fabrics, and two-feldspar geothermometry of asymmetric strain-induced myrmekite range between ~400 and 650 °C. Micro- and macro-kinematic indicators suggest west-directed displacement dominated over this temperature range. Mean kinematic vorticity estimates record early pure shear dominated flow (49–66% pure shear) overprinted by later simple shear (1–57% pure shear), high-strain (36–50% shortening and 57–99% down-dip extension) dominated flow during the later increments of ductile deformation. Exhumation of the massif was accommodated by at least ~21–42 km of displacement on the Ama Drime detachment. Samples from the Nyönno Ri detachment were exhumed from similar depths. We propose that exhumation on the Nyönno Ri detachment during initiation of orogen-parallel extension (11–13 Ma) resulted in a west-dipping structural weakness in the footwall that reactivated as the Ama Drime detachment.

© 2010 Elsevier Ltd. All rights reserved.

1. Introduction

Continental collision between the Indian and Asian plates from the Eocene to Holocene resulted in profound crustal shortening and thickening that produced the Himalaya and Tibetan Plateau. Previous studies (e.g. Grujic, 2006; Grujic et al., 1996, 2002; Vannay and Grasemann, 1998; Grasemann et al., 1999; Hodges et al., 1992, 2001) have largely focused on the southward propagation or extrusion of the Greater Himalayan Series (GHS) from the Eocene to middle Miocene during continental convergence (Fig. 1). Southward flow was accommodated by coeval movement on the South Tibetan detachment system (STDS) on top of the GHS and the Main Central thrust zone (MCTZ) at the bottom (Fig. 1) (Nelson et al., 1996; Searle et al., 2006).

After the middle Miocene, a transition from south-directed mid-crustal flow to orogen-parallel extension occurred in the Himalaya that resulted in the formation of north–south striking normal faults, graben, and domes that often offset or reactivate the STDS and/or the MCTZ (Fig. 1) (Murphy et al., 2002; Kapp and Guynn, 2004; Murphy and Copeland, 2005; Theide et al., 2005, 2006; Jessup et al., 2008a; Jessup and Cottle, in press). Structural, geochronologic and thermochronometric data from the Leo Pargil dome, the Gurla Mandhata core complex, and the Ama Drime Massif (ADM) demonstrate that faults and shear zones that accommodated crustal shortening (i.e. the STDS and MCTZ) between the Eocene and early Miocene are now inactive and are therefore no longer capable of accommodating south-directed mid-crustal flow (Cottle et al., 2007; Murphy, 2007).

The ADM is a ~30-km-wide north–south striking antiformal structure that narrows towards the north and is located ~50 km northeast of Mount Everest. It is bound by the north–south striking Nyönno Ri detachment (NRD) on the eastern flank and the north–south trending Ama Drime detachment (ADD) on the western flank (Figs. 1 and 2) (Jessup et al., 2008a). To the north, the NRD transitions into the Xainza-Dinggyê graben that offsets the STDS (Burchfiel et al., 1992; Zhang and Guo, 2007) and is kinematically linked to east–west extension in the interior of the plateau (Taylor et al., 2003). Structural, petrologic, and geochronologic data

* Corresponding author.
E-mail address: jlangill@utk.edu (J.M. Langille).

0191-8141/$ – see front matter © 2010 Elsevier Ltd. All rights reserved.
doi:10.1016/j.jsg.2010.04.005

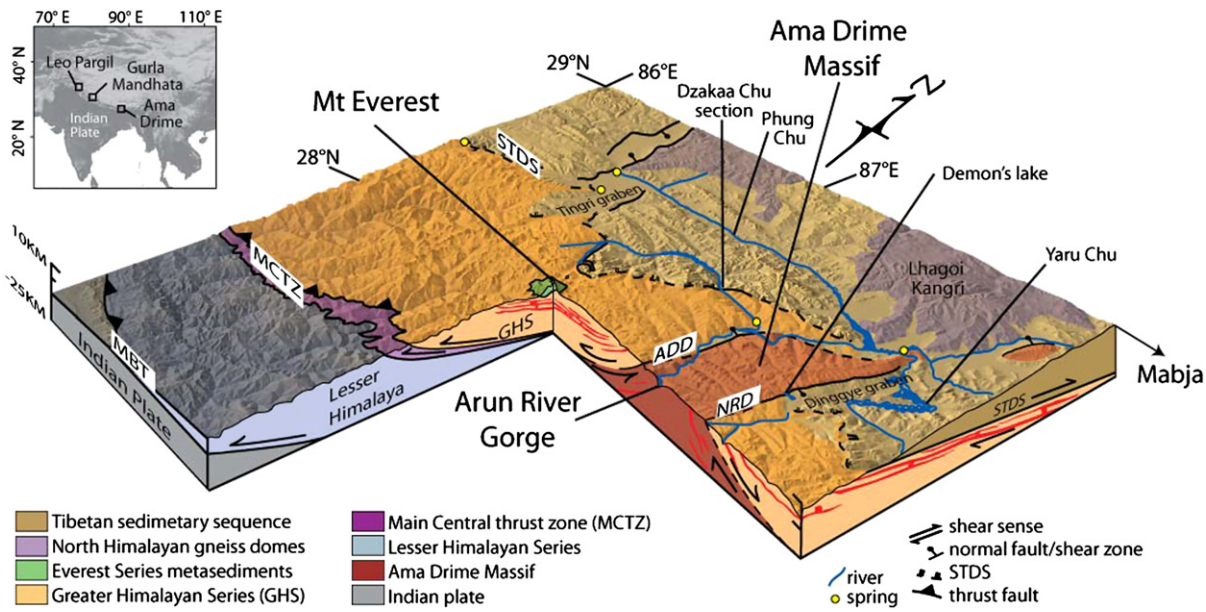

Fig. 1. Simplified interpretive block diagram of the Everest region. STDS, South Tibetan detachment system; MBT, Main Boundary thrust; MHT, Main Himalayan thrust; ADD, Ama Drime detachment; NRD, Nyönno Ri detachment. After Jessup et al. (2008a) and Searle et al. (2006).

indicate that the antiformal structure of the ADM is the result of evolving mid-crustal flow along the southern margin of the Tibetan Plateau (Jessup et al., 2008a; Cottle et al., 2009a). This study presents new kinematic, microstructural, and vorticity data from three transects across the ADD on the western flank of the ADM along with one transect from the NRD on the eastern flank. These data provide new constraints on the role of strain partitioning and shear zone development associated with orogen-parallel extension in a convergent setting. We integrate these new data with existing data to propose a model for the evolution of the ADM.

2. Geologic setting

2.1. Regional geology

The geology in the Mount Everest region, southwest of the ADM can be grouped into three main fault-bounded litho-tectonic units. In order of increasing structural position these include (from south to north); the Lesser Himalayan Series (LHS), the GHS, and the Tibetan Sedimentary Series (TSS). These units are separated by three north dipping fault systems; the Main Boundary thrust (MBT), the MCTZ, and the STDS (Fig. 1). The MCTZ and the MBT are inferred, based on geophysical data, to sole into the Main Himalayan thrust (MHT) to the north beneath the Tibetan Plateau (Nelson et al., 1996; Searle et al., 2006). Below the MHT (35–75 km) the lower crust is composed of Archean Indian shield granulite facies rocks (Searle et al., 2006).

The 20-km-thick LHS, bound between the MBT below and the MCTZ above, consists of Paleo- to Mesoproterozoic metamorphosed clastic sediments and gneiss (Brookfield, 1993; Pognante and Benna, 1993; Goscombe et al., 2006). The Neoproterozoic to Cambrian GHS is bound at the base by the MCTZ and at the top by the STDS. The upper GHS is separated from the lower GHS by the High Himalayan thrust (HHT) (Goscombe et al., 2006). The lower GHS is bound between the HHT and the base of the MCTZ. The upper GHS structurally overlies metapelitic schists and the Ulleri and Num orthogneisses in the lower GHS (within the MCTZ) (Searle et al., 2008). In contrast, others (e.g. Goscombe et al., 2006) place the Ulleri orthogneiss in the LHS. The GHS is composed of a ~28-km-thick section of metapelitic rocks, augen gneiss, calc-silicates, and marble that was metamorphosed to amphibolite facies and intruded by Miocene sills and dikes (Hodges, 2000; Searle et al., 2003; Viskupic et al., 2005).

South of Mount Everest, in the Dudh Kosi drainage, the maximum age for movement along the MCTZ is constrained by $^{40}Ar/^{39}Ar$ hornblende and $^{208}Pb/^{232}Th$ monazite geochronology and indicates that amphibolite-facies metamorphism of hanging wall rocks occurred at 22 ± 1 Ma (Hubbard and Harrison, 1989) and potentially as early as 24–29 Ma (Catlos et al., 2002). The GHS in the Everest region experienced an early kyanite-grade event (550–680 °C and 0.8–1.0 GPa) at 38.9 ± 0.9 Ma that is a record of crustal thickening (Pognante and Benna, 1993; Cottle et al., 2009b). Kyanite-grade metamorphism was overprinted by a high-temperature low-moderate-pressure sillimanite-grade event (650–750 °C and 0.4–0.7 GPa) associated with decompression melting and granite emplacement between 28.0 and 22.6 Ma (Pognante and Benna, 1993; Simpson et al., 2000; Searle et al., 2003; Viskupic et al., 2005; Jessup et al., 2008b; Cottle et al., 2009b). $^{40}Ar/^{39}Ar$ biotite ages from the GHS are <14 Ma, suggesting that metamorphism in the interior portion of the GHS had ceased by this time (Viskupic et al., 2005).

Timing constraints on the STDS in the Mount Everest region suggest that the system was active until 18–16 Ma (Hodges et al., 1992; Murphy and Harrison, 1999; Searle et al., 2003). In the Dzakaa Chu section of the STDS (Figs. 1 and 2), U–Th–Pb geochronology conducted on a leucogranite dike that crosscuts the mylonitic fabric within the lower part of the STDS suggests that fabric development in this section of the shear zone occurred at <20 Ma (Cottle et al., 2007). In the Dinggyê graben, the ductile portion of the footwall rocks ~100 m below the STDS brittle detachment were active until ~15–16 Ma (Leloup et al., 2010).

The structurally highest unit, the TSS, consists of Proterozoic to Jurassic pre-, syn-, and post-rift sedimentary rocks, a Jurassic to Cretaceous passive continental margin sedimentary sequence, and an upper Cretaceous to Eocene syn-collisional sedimentary sequence (Gansser, 1964; Le Fort, 1975; Gaetani and Garzanti, 1991; Brookfield, 1993; Liu and Einsele, 1994; Garzanti, 1999). Middle Miocene to Holocene north–south striking normal faults cut these

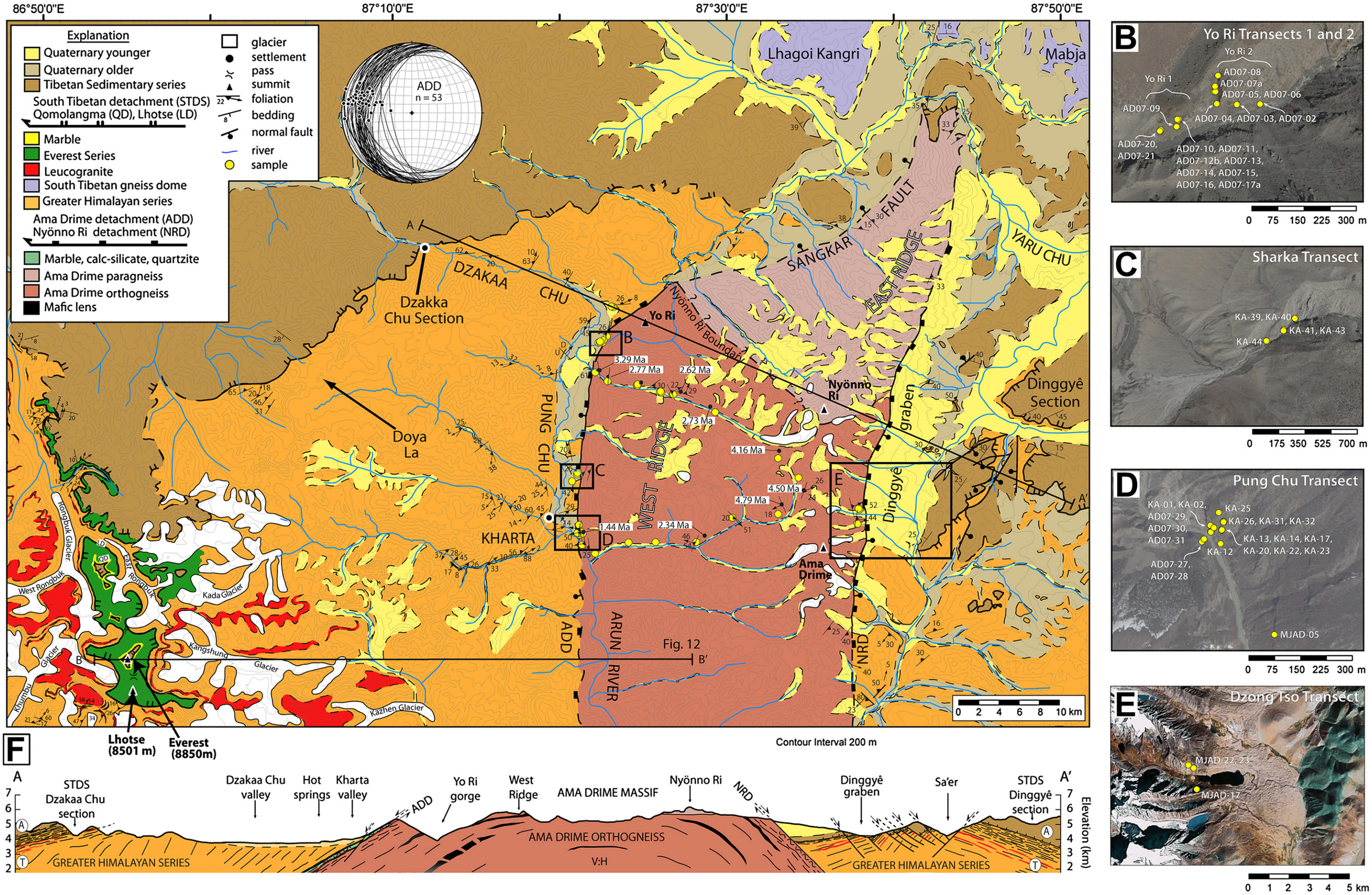

Fig. 2. (A) Geologic map of the Ama Drime Massif (Jessup et al., 2008c) and Mount Everest (Jessup et al., 2008b) including structural data and sample locations after Jessup et al. (2008a,b). Aside from the Nyönno Ri Detachment (NRD), data from the eastern side is after Burchfiel et al. (1992). Structural data at the nose of the massif, the NRD, and the Sangkar Fault after Kali et al. (2010). Everest data and map from Jessup et al. (2008b), Hubbard and Harrison (1989), Murphy and Harrison (1999) and, Searle et al. (2003). Nyönno Ri Boundary after Kali et al. (2010). ADD, Ama Drime Detachment. (B) Location map of the Yo Ri 1 and Yo Ri 2 transect samples. (C) Location map of the Sharka transect samples. (D) Location map of the Pung Chu transect samples. (E) Location map of Demon's Lake and Dzong Tso transect samples. Arial imagery in (B) through (E) from google. (F) Geologic cross section through the Ama Drime Massif. Cross section location shown in (A). Not the same scale as the map. Modified from Jessup et al. (2008a).

older structures forming a series of graben that are characteristic of the southern Tibetan Plateau (e.g. Armijo et al., 1986; Wu et al., 1998; Stockli et al., 2002; Taylor et al., 2003; Dewane et al., 2006; Hager et al., 2006; Zhang and Guo, 2007).

2.2. Geology of the Ama Drime Massif

The ADM is a NNE-trending antiformal structure that is composed of the Ama Drime orthogneiss to the south and the Ama Drime paragneiss to the north (Fig. 2) (Kali et al., 2010) that are separated by the relatively unexplored Nyönno Ri Boundary (Fig. 2) (Kali et al., 2010).

The western flank of the ADM is defined by the ~100–300-m-thick, west-dipping ADD that is composed of schist, leucogranite, calc-silicate, quartzite, and marble that records solid-state fabric development (Jessup et al., 2008a). The shear zone separates migmatitic orthogneiss of the GHS in the hanging wall from the granulite facies (750 °C and 0.7–0.8 GPa), migmatitic Ama Drime orthogneiss in the footwall (Fig. 3A–C) (Jessup et al., 2008a; Cottle et al., 2009a). The shear zone rocks record polyphase folding of a pervasive foliation that is interpreted to record earlier deformation associated with movement on this contact (Jessup et al., 2008a). Rocks within the shear zone preserve a well-developed S–C fabric with a down-dip stretching lineation and are locally folded. Layers of ultra-mylonite are parallel to the main mylonitic fabric (Fig. 3D). These ductile features are offset by at least one brittle detachment (Fig. 3E) filled with fault gouge. Veins of pseudotachylite truncate the mylonitic fabric at high angles and contain fragments of the host rock (Fig. 3F). $^{40}Ar/^{39}Ar$ biotite ages from the mylonitic footwall suggest that the ADD was active between 10 and 6 Ma (Kali et al., 2010). Towards the north, the ADD transitions into the Sangkar fault (also termed the Pum Qu fault by Armijo et al., 1986) (~12 Ma $^{40}Ar/^{39}Ar$ muscovite age) and eventually to the nose of the ADM (the hinge of the antiform) where faults have a minimum displacement (Fig. 2) (Kali et al., 2010).

The south-central portion of the ADM is composed of Ama Drime orthogneiss that is variably migmatized (12.8 ± 0.2 Ma) and dominated by melt-present deformation features (Cottle et al., 2009a; Kali et al., 2010). Protolith ages for the Ama Drime orthogneiss (1799 ± 9 Ma) may correlate to the Ulleri orthogneiss that is interpreted to be at the base of GHS, below the HHT in the hanging wall of the MCTZ (Cottle et al., 2009a; Searle et al., 2008), or in the underlying LHS (e.g. Goscombe et al., 2006). Mafic lenses cored by granulitized eclogite are surrounded by orthogneiss that experienced muscovite dehydration melting (Lombardo et al., 1998; Lombardo and Rolfo, 2000; Groppo et al., 2007; Guillot et al., 2008) and anatexis at <13.2 ± 1.4 Ma (Cottle et al., 2009a). Melt-filled fractures that break a boudinaged mafic lens were emplaced at 11.6 ± 0.4 Ma and record top-to-the-west shearing during the initial stages of orogen-parallel extension (Cottle et al., 2009a). Other mafic layers are crosscut by pegmatite dikes (9.8 ± 1.2 Ma) on the eastern side of the interior portion of the ADM (Kali et al., 2010).

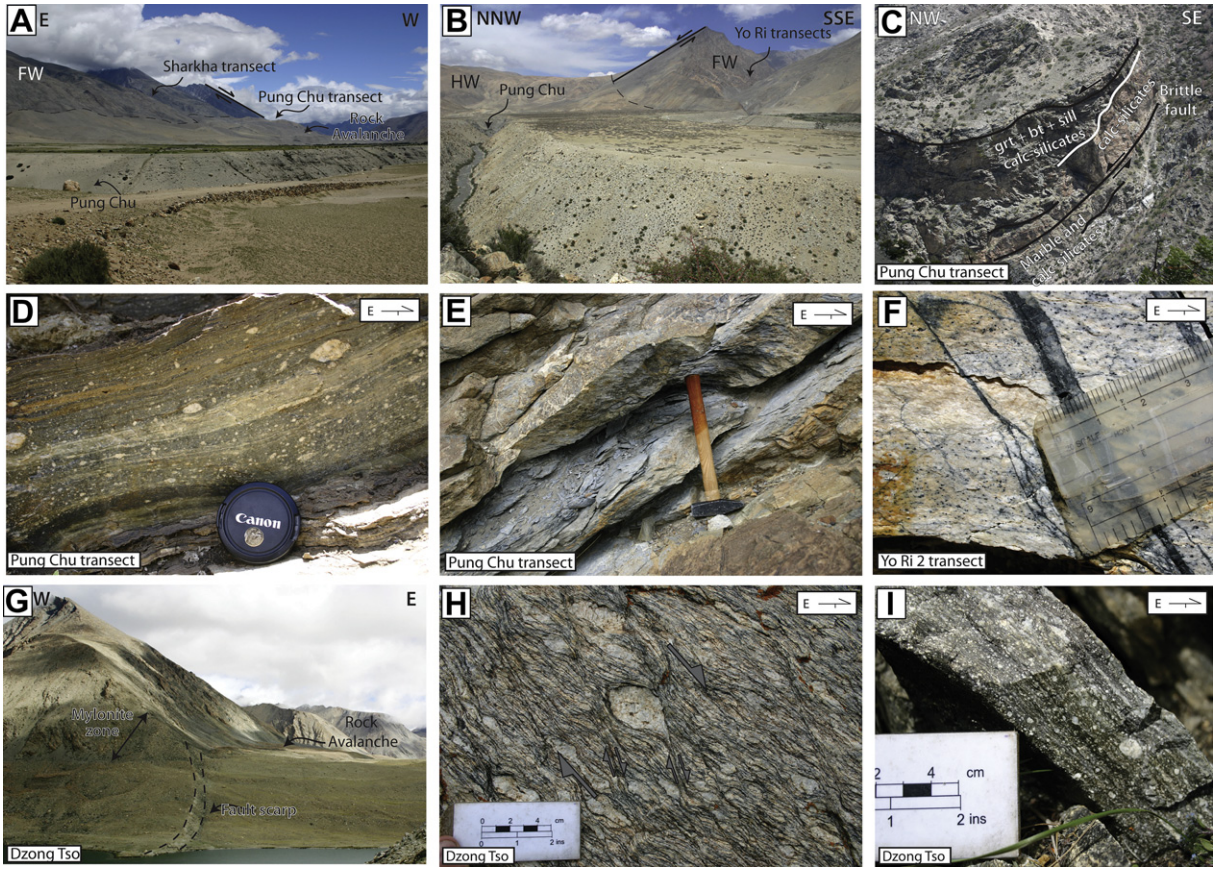

Fig. 3. (A) View of the Pung Chu and Sharka transects looking south. (B) View of the Yo Ri transects looking northeast. (C) Exposure of the ADD shear zone exposed in the Pung Chu transect. Black lines represent the shear zone boundary and brittle faults. White lines represent lithologic contacts. (D) Example of a mylonitic calc-silicate exposed within the Pung Chu transect that records top-to-the-west sense of shear. (E) Brittle fault filled with fault gouge exposed within the Pung Chu transect. (F) Pseudotachylite within leucogranite near the Yo Ri 2 transect. (G) View of a fault scarp offsetting Quaternary deposits, looking north from Dzong Tso (Demon's Lake) on the eastern flank of the ADM. (H) Augen gneiss on the eastern limb of the ADM exposed north of Demon's Lake. Asymmetric tails indicate top-to-the-east sense of shear. (I) Mylonite containing feldspar porphyroclasts exposed along the NRD.

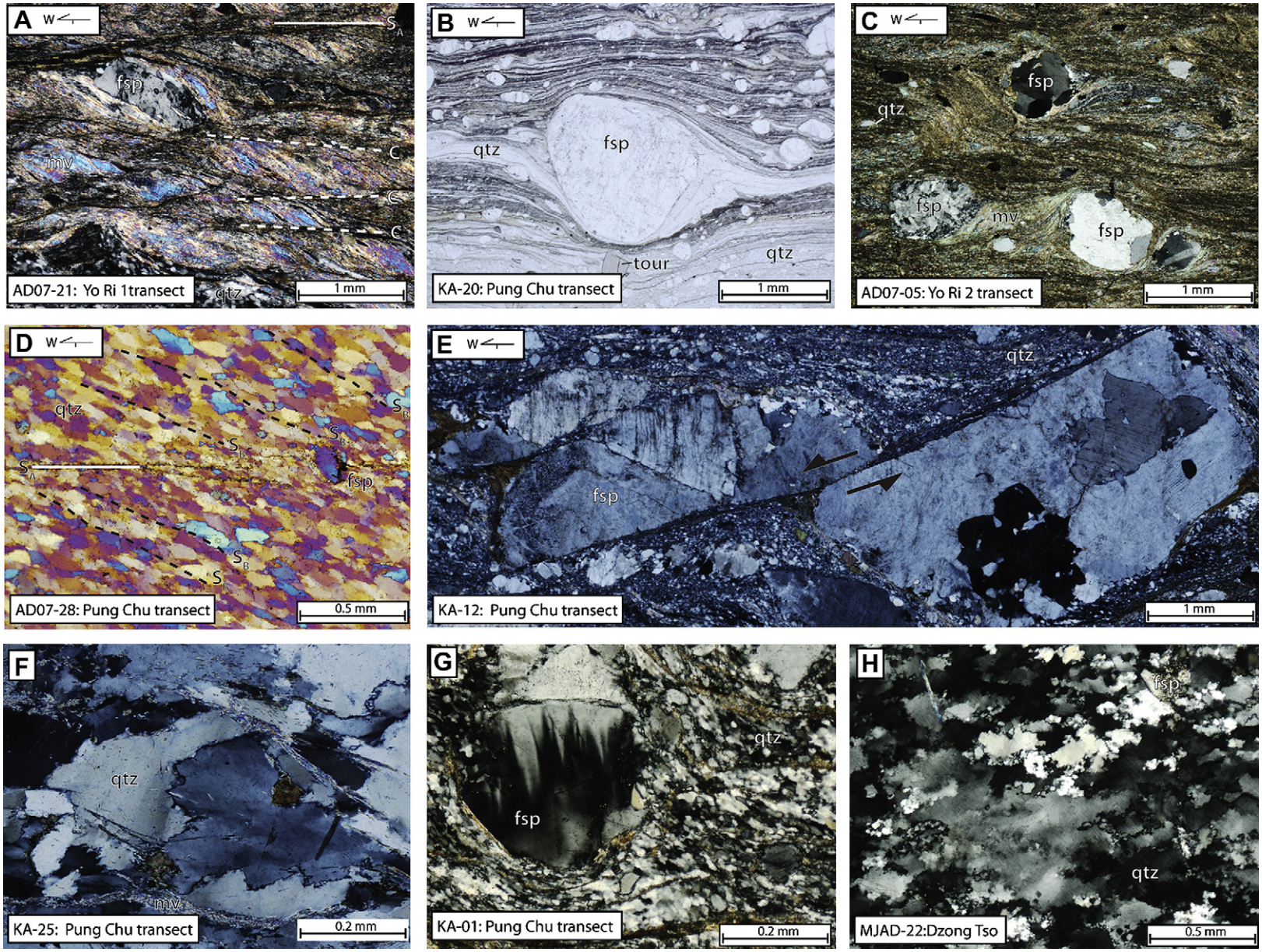

Fig. 4. Photomicrographs of kinematic indicators from the ADD transects, (A) through (E), and quartz and feldspar deformation textures, (F) through (H). (A) Mica fish that record top-to-the-west sense of shear; cross polars. S_A, main foliation; C, C-type shear bands; fsp, feldspar; mv, muscovite. (B) δ-type strain shadow on a feldspar porphyroclast indicating top-to-the-west sense of shear; plane light. qtz, quartz; tour, tourmaline. (C) σ-type strain shadows on feldspar porphyroclasts indicating top-to-the-west sense of shear, cross polars. (D) Quartz grain shape foliation (S_B) indicating top-to-the-west sense of shear; cross polars with gypsum plate inserted. (E) Shear band type offset feldspar porphyroclast suggesting top-to-the-west sense of shear; cross polars. (F) Quartz exhibiting bulging (BLG) recrystallization at quartz grain boundaries indicating deformation temperatures of 280–400 °C overprinting a higher temperature fabric, cross polars. (G) Quartz exhibiting Sub-Grain Rotation (SGR) recrystallization indicating deformation temperatures between 400 and 500 °C. Flame perthite in a rigid feldspar porphyroclast also indicates deformation temperatures between 400 and 500 °C; cross polars. (H) Quartz exhibiting Grain-Boundary Migration (GBM) recrystallization indicating deformation temperatures of 500–650 °C; cross polars.

Exhumation rates of 2.2 ± 0.2 mm/yr from 0.7 and 0.8 GPa between ~13 and 2 Ma (Cottle et al., 2009a) were accommodated by the development of the ADD and NRD during orogen-parallel extension. (U–Th)/He apatite ages from the central portion of the ADM define an exhumation rate of ~1 mm/yr between 1.4 and 4.2 Ma that records continued exhumation with movement on the ADD and NRD (Jessup et al., 2008a; Kali et al., 2010).

The NRD is composed of a system of shear zones and faults that occur within the Ama Drime orthogneiss and paragneiss and defines the eastern limb of the ADM (Jessup et al., 2008a). Hanging wall rocks have been removed by normal faulting in the Dinggyê graben. 1-km-tall triangular facets extend above Dzong Tso where moraine deposits are offset by a fault scarp with ~5 m of throw and an apparent normal displacement (Jessup et al., 2008a) (Fig. 3G). A decrease in the height of the triangular facets towards the north is interpreted as evidence for decrease in displacement along the NRD towards the north (Kali et al., 2010).

Footwall rocks record a steepening of the main foliation 25–45° towards the shear zone where they preserve a mylonite zone with a pervasive S–C fabric and down-dip stretching lineation that records top-to-the-east sense of shear (Burchfiel et al., 1992; Jessup et al., 2008a). Near Dzong Tso (Demon's Lake), footwall rocks are well-exposed and contain a ~100–300-m-thick mylonite zone that strikes north–south, dips ~45° east, and preserves a down-dip stretching lineation (Fig. 3G) (Jessup et al., 2008a). Migmatitic orthogneiss exposed at deeper structural positions record melt-present high-temperature fabric development. At structurally shallower positions, feldspar grains begin to act as semi-rigid bodies suggesting deformation at moderate temperatures (Fig. 3H). Rigid feldspar porphyroclasts suspended in a fine-grained matrix of aligned recrystallized quartz and phyllosilicates mark narrow zones of mylonite and ultra-mylonite that are sub-parallel to the main shear zone fabric (Fig. 3I). An undeformed leucogranite dike (11 ± 0.4 Ma) that crosscuts the NRD footwall mylonites provides a minimum age for fabric development (Kali et al., 2010). $^{40}Ar/^{39}Ar$ muscovite and biotite ages of 10–13 Ma indicate the onset of east–west extension and exhumation after the cessation of movement on the STDS in this region (Zhang and Guo, 2007; Leloup et al., 2010; Kali et al., 2010).

3. Shear sense indicators

Oriented samples were collected from three transects across the ADD and one from the NRD. Along the ADD, from north to south these transects include the Yo Ri (1 and 2), the Sharkha, and the Pung Chu transects (Fig. 2A–D). The Dzong Tso transect crosses the NRD on the eastern limb of the range (Fig. 2E). Samples were cut parallel to the lineation and perpendicular to the foliation (*XZ* section). C- (Fig. 4A) and C′-type shear bands, mica fish (Fig. 4A), σ- and δ-type asymmetric tails on porphyroclasts (Fig. 4B and C), oblique quartz grain shape foliation (Fig. 4D), and shear folds were used to determine the spatial distribution of shear sense in samples collected from three transects across the ADD and one across the NRD. Electron backscatter diffraction (EBSD) analysis was used to generate quartz lattice-preferred orientation (LPO) diagrams, from which the asymmetry of the [*c*] and ⟨*a*⟩ axes patterns with respect to the foliation and lineation was also used to determine shear sense (Figs. 5A and 6) (e.g. Lister and Hobbs, 1980; Law, 1990). Diffraction patterns were collected using an FEI Quanta 400 FEG scanning electron microscope coupled with a HKL Nordlys 2 EBSD camera at the University of California, Santa Barbara. CHANNEL 5 HKL software was used to index the diffraction patterns with Hough resolution of 80, detecting 7–8 bands with standard divergence and a quartz structure file containing 60 reflectors.

3.1. Results

The Pung Chu transect is the southernmost transect across the ADD and contains marble, schist, calc-silicate, leucogranite, and quartzite (Fig. 2d). δ- and σ-type asymmetric tails on feldspar (Fig. 4B) and diopside porphyroclasts, mica fish, oblique quartz grain shape foliation (Fig. 4D), C- and C′-type shear bands, shear-band type offset porphyroclasts (Passchier and Trouw, 2005) (Fig. 4E), and quartz LPO patterns (Fig. 6A) preserved in samples from this transect (Figs. 2B and 3A) consistently record top-to-the-west shear sense (Table 1). Samples AD07-27 and MJAD-05 are exceptions to this trend and exhibit σ-type strain shadows, C′-type shear bands, mica fish, and quartz [*c*] and ⟨*a*⟩ axis LPO patterns which indicate top-to-the-east sense of shear (Fig. 6A; Table 1). MJAD-05 was collected ~1 km from the remainder of the Pung Chu samples in an ultra-mylonite zone that dips steeply to the east (355, 72E), contains a down-dip stretching lineation, and records top-to-the-east displacement. This is the only steeply dipping mylonite zone that was documented in the more internal portion of the range.

Samples along the Sharkha transect are composed of calc-silicate, quartzite, and deformed leucogranite that contain σ-type asymmetric tails on feldspar porphyroclasts and mica fish that record top-to-the-west sense of shear (Table 1). Quartz [*c*] and ⟨*a*⟩ LPO axes patterns from samples KA-39 and KA-41 (Fig. 6B) also confirm top-to-the-west sense of shear (Table 1).

σ-type strain shadows on feldspar porphyroclasts and mica fish (Fig. 4A) within quartzite and vein quartz along the Yo Ri 1 transect (Fig. 2B and 3B) record top-to-the-west sense of shear; the exception being AD07-15, which contains σ-type strain shadows on feldspar porphyroclasts and mica fish that indicate top-to-the-east sense of shear (Table 1). Quartz [*c*] and ⟨*a*⟩ axis LPO patterns from samples AD07-21, AD07-17a, and AD07-12b consistently define top-to-the-west sense of shear (Fig. 6C; Table 1).

In the Yo Ri 2 transect (Figs. 2B and 3B), σ-type strain shadows on feldspar and diopside porphyroclasts (Fig. 4C), mica fish, C′-type shear bands, and drag folds within quartzite, calc-silicate, gneiss, and deformed leucogranite record top-to-the-west sense of shear. One exception is AD07-04, which has a poorly developed grain shape foliation, mica fish, and a quartz [*c*] and ⟨*a*⟩ axis LPO indicating top-to-the-east sense of shear (Fig. 6D; Table 1). The quartz [*c*] and ⟨*a*⟩ axis LPO patterns from sample AD07-02 suggest top-to-the-west sense of shear (Fig. 6D; Table 1).

Within the NRD near Dzong Tso (Fig. 2E), σ-type tails on feldspar porphyroclasts, mica fish, quartz grain shape foliation, and drag folds within three samples, two mylonitic gneiss and one schist, indicates top-to-the-east sense of shear (Table 1).

4. Deformation temperatures

Deformation temperatures during the development of the kinematic indicators and quartz LPO fabrics mentioned above were estimated using; (1) recrystallized quartz and feldspar deformation microstructures (e.g. Jessell, 1987; Hirth and Tullis, 1992; Fitz Gerald and Stünitz, 1993; Lloyd and Freeman, 1994; Hirth et al., 2001; Stipp et al., 2002a,b), (2) the opening angle of quartz [*c*] axis LPOs (Kruhl, 1998; Law et al., 2004), (3) quartz slip systems (e.g. Mainprice et al., 1986; Tullis and Yund, 1992), and (4) two-feldspar geothermometry (Stormer, 1975; Whitney and Stormer, 1977; Simpson and Wintsch, 1989).

4.1. Quartz and feldspar microstructures

Quartz exhibits bulging (BLG) recrystallization at temperatures of 280–400 °C (Stipp et al., 2002a, b) (Fig. 4F), Sub-Grain Rotation

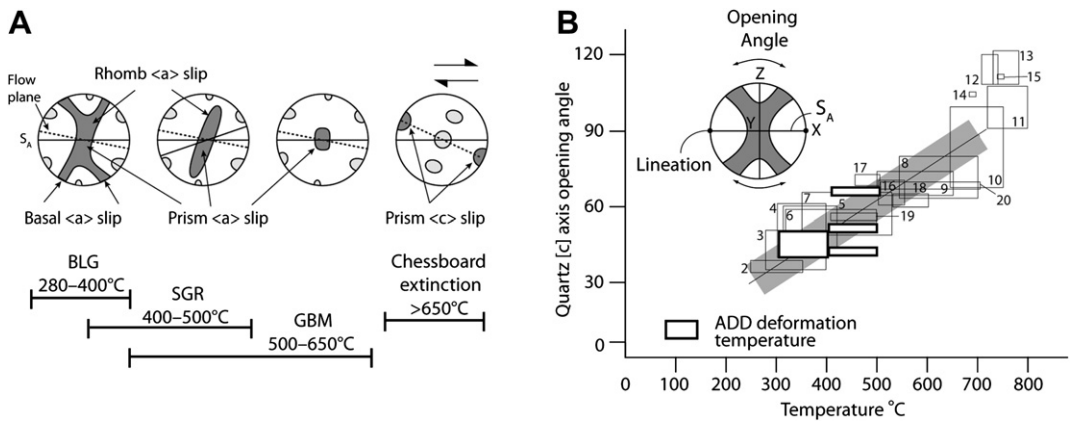

Fig. 5. (A) Simplified stereonets showing the dependence of quartz LPOs and inferred slip systems on increasing temperature during noncoaxial deformation and plane strain (see text). [*c*] axes are shown in dark grey and ⟨*a*⟩ axes in light grey. Modified from Passchier and Trouw (2005). (B) Relationship between [*c*] axis opening angle to temperature. Grey line is the best fit line with ± 50 °C error. *X*, *Y*, and *Z* strain axes are shown. Boxes 1–15: from Kruhl (1998); 16: Law et al. (1992); 17: Nyman et al. (1995); 18: Okudaira et al. (1995); 19 and 20: Langille et al. (2010). Data from this study are shown. Modified from Law et al. (2004).

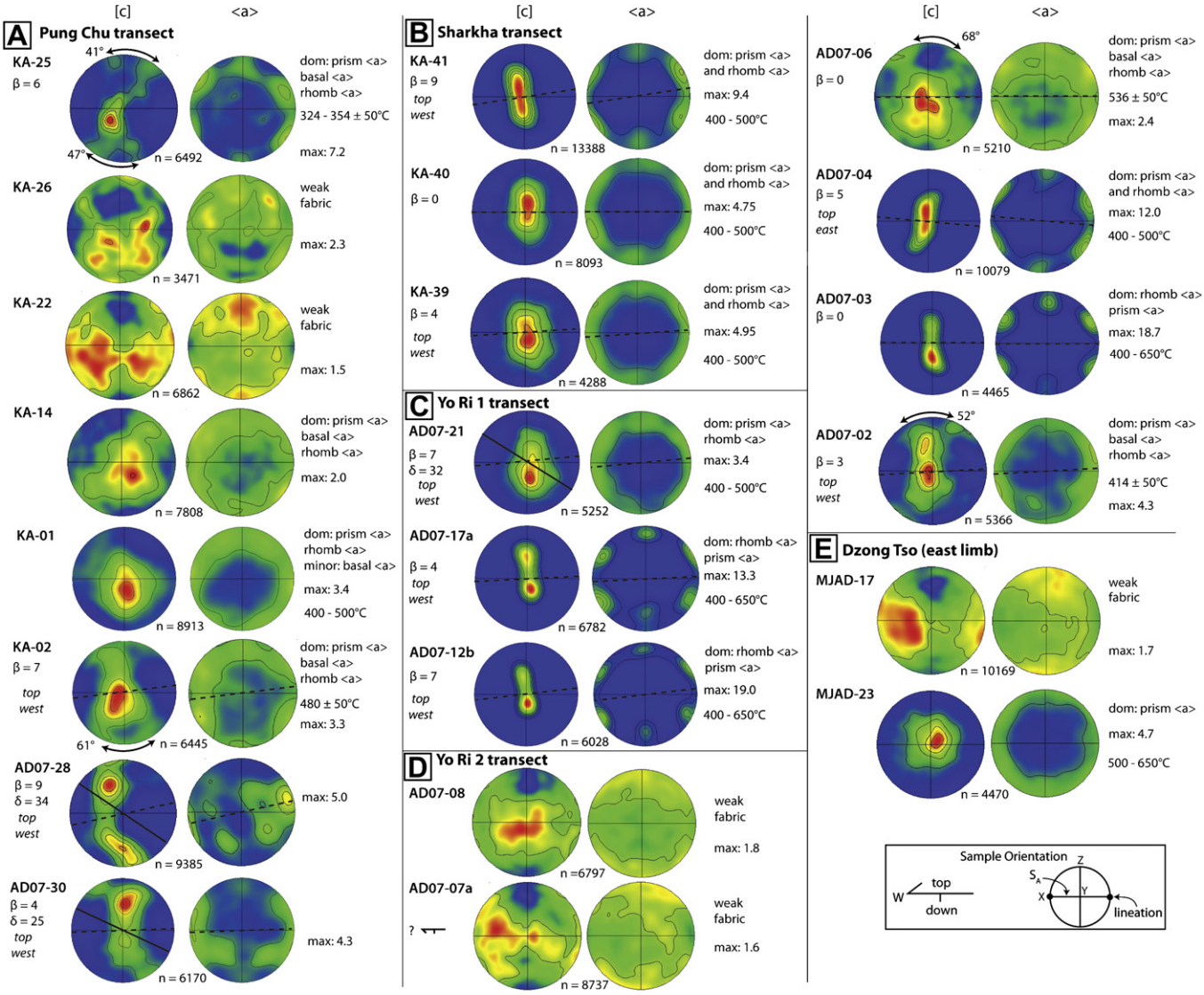

Fig. 6. EBSD-generated quartz lattice-preferred orientations (LPO) in order of increasing structural depth for the (A) Pung Chu, (B) Sharka, (C) Yo Ri 1, (D) Yo Ri 2, and (E) Dzong Tso transects. Upper hemisphere [*c*] and ⟨*a*⟩ axis stereonet plots shown. Opening angle and corresponding deformation temperature, quartz texture derived deformation temperature, flow plane (dashed line), quartz grain shape foliation (S_B, solid line), angle between foliation (S_A) and flow plane (β), angle between S_A and S_B (δ), shear sense, quartz slip systems (dom, dominant slip system), and number (*n*) of quartz grains measured noted. All plots oriented as indicated in the sample orientation box. Data are point-per grain; contouring based on mean uniform density (m.u.d.) with maximum (max) values indicated.

Table 1
Summary of shear sense, vorticity, and temperature data.

Sample	Rock type	Shear sense	W_m RGN	W_m GSF	R_{xz}	Deformation temperature (°C)	Temperature indicator[d]
Pung Chu transect							
KA-25[a]	qtz	t-E[c]	–	–	–	324 ± 50, 354 ± 50, 280–400	o.a., s.s.
KA-31	mbl	–	–	–	–	400–500	–
KA-26[a]	sch	t-W[c]	–	–	–	400–500	–
KA-32	c.s.	–	–	–	–	400–500	–
KA-17	mbl	t-W[c]	0.60–0.65	–	–	400–500	–
KA-20	qtz	–	0.56–0.57	–	–	400–500	–
KA-22[a]	c.s.	t-W[c]	0.57–0.63	–	–	400–500	–
KA-23	mbl	t-W[c]	0.54–0.62	–	–	400–500	–
KA-14[a]	c.s.	t-W[c]	0.52–0.58	–	–	400–500	–
KA-13	c.s.	t-W[c]	0.56–0.59	–	–	400–500	–
KA-01[a]	qtz	t-W[c]	0.69–0.72	–	–	400–500	s.s.
KA-02[a]	qtz	t-W,[b] t-W[c]	0.52–0.55	–	–	480 ± 50, 400–500	o.a., s.s.
KA-12	qtz	t-W[c]	0.53–0.61	–	–	400–500	–
AD07-28[a]	qtz	t-W,[b] t-W[c]	0.57–0.59	0.93–0.99	10.6–27	400–500	–
AD07-29a	c.s.	–	–	–	–	400–500	–
AD07-29b	c.s.	t-W[c]	–	–	–	400–500	–
AD07-30[a]	qtz	t-W,[b] t-W[c]	0.54–0.61	0.62–0.84	6.4–19.2	400–500	–
AD07-31	qtz	t-W[c]	–	–	–	400–500	–
AD07-27	c.s.	t-E[c]	–	–	–	400–500	–
MJAD-05	c.s.	t-E[c]	–	–	–	400–500	–
Sharka transect							
KA-44	c.s.	t-W[c]	0.50–0.58	–	–	400–500	–
KA-41[a]	c.s.	t-W,[b] t-W[c]	0.55–0.59	–	–	400–500	–
KA-43	qtz	–	–	–	–	400–500	–
KA-39[a]	leuc	t-W,[b] t-W[c]	–	–	–	400–500	–
KA-40[a]	c.s.	t-W[c]	0.57–0.61	–	–	369–435, 400–500	f.g.
Yo Ri 1 transect							
AD07-20	qtz	t-W[c]	–	–	–	400–500	–
AD07-21[a]	qtz	t-W,[b] t-W[c]	0.57–0.64	0.74–0.98	6.7–24	400–500	s.s.
AD07-17a[a]	qtz	t-W,[b] t-W[c]	–	–	–	400–650	s.s.
AD07-16	qv	–	–	–	–	400–500	–
AD07-15	qv	t-E[c]	–	–	–	400–500	–
AD07-14	qv	t-W[c]	–	–	–	400–500	–
AD07-13	qv	t-W[c]	–	–	–	400–500	–
AD07-12b[a]	qv	t-W,[b] t-W[c]	–	–	–	400–650	s.s.
AD07-10	qv	t-W[c]	–	–	–	400–500	–
AD07-11	qv	t-W[c]	0.52–0.55	–	–	500–650	–
AD07-09	qv	t-W[c]	–	–	–	400–500	–
Yo Ri 2 transect							
AD07-08[a]	qtz	t-W[c]	0.53–0.60	–	–	500–650	s.s.
AD07-07a	c.s.	–	0.61–0.65	–	–	400–500	–
AD07-05	c.s.	t-W[c]	0.57–0.63	–	–	500–650	–
AD07-06[a]	leuc	t-W[c]	–	–	–	537 ± 50, 400–500	o.a., s.s.
AD07-04[a]	qtz	t-E,[b] t-E[c]	–	–	–	400–500	s.s.
AD07-03[a]	qtz	t-W[c]	–	–	–	400–650	s.s.
AD07-02[a]	gns	t-W,[b] t-W[c]	–	–	–	414 ± 50, 400–500	o.a., s.s.
Dzong Tso transect (east limb)							
MJAD-17[a]	sch	t-E[c]	–	–	–	400–500	–
MJAD-22	gns	t-E[c]	–	–	–	500–650	–
MJAD-23[a]	gns	t-E[c]	–	–	–	500–650	s.s.

Abbreviations: qtz, quartzite; qv, quartz vein; mbl, marble; c.s., calc-silicate; sch, schist; leuc, leucogranite; gns, gneiss; t-E, top-to-the-east; t-W, top-to-the-west. Samples are in order of increasing structural depth per transect.

[a] Sample analyzed with EBSD.
[b] Shear sense determined from EBSD-generated quartz LPO data.
[c] Shear sense determined from microstructural geometries.
[d] All samples utilized quartz and feldspar deformation textures. o.a., opening angle; s.s., quartz LPO slip systems; f.g., feldspar geothermometry.

(SGR) recrystallization at temperatures of 400–500 °C (Stipp et al., 2002a, b) (Fig. 4G), and Grain-Boundary Migration (GBM) recrystallization (Fig. 4H) at temperatures of >500 °C (Stipp et al., 2002a, b). At temperatures >650 °C quartz exhibits chessboard extinction (e.g. Lister and Dornsiepen, 1982). At deformation temperatures where quartz experiences BLG recrystallization, feldspar deforms by brittle fracturing. At temperatures where quartz experiences SGR recrystallization, feldspar deforms by internal microfracturing with minor dislocation glide (Pryer, 1993). Flame perthite is also common in albite porphyroclasts at these temperatures (Fig. 4G) (Pryer, 1993). At quartz GBM recrystallization conditions, feldspar deforms by microfracturing. However, dislocation glide and BLG recrystallization can occur in feldspar at higher temperatures (Tullis and Yund, 1991).

4.2. Opening angle and quartz [c] axis lattice-preferred orientations

The opening angle is defined as the angle between the girdles measured in the plane perpendicular to foliation and parallel to lineation (*XZ* section) (Fig. 5B) (Kruhl, 1998). Experimental studies (e.g. Tullis et al., 1973; Lister et al., 1978; Lister and Hobbs, 1980; Lister and Dornsiepen, 1982; Wenk et al., 1989) indicate that the

opening angle of quartz [*c*] axis LPOs increases with increasing deformation temperature (Fig. 5B). The opening angle was used to calculate the deformation temperature with an error of ±50 °C (Kruhl, 1998). Other factors such as strain rate also play a role in the development of the opening angle (Tullis et al., 1973).

Our deformation temperatures derived from quartz and feldspar recrystallization textures were plotted against the opening angle for samples KA-25, KA-02, AD07-06, and AD07-02 (Fig. 5B). In addition, deformation temperatures estimated from quartz and feldspar recrystallization textures from the Mabja Dome (Fig. 2) (Langille et al., 2010) are also plotted against opening angle (boxes 19–20, Fig. 5B). These data provide an independent confirmation of the relationship between increasing opening angle and deformation temperature between ~300 and 700 °C (Fig. 5B).

Temperatures defining the transition from prism ⟨*a*⟩ slip to prism [*c*] slip, expressed as a maxima in the *Y*-direction and maxima parallel to lineation (Fig. 5A), respectively, in quartz are well constrained (e.g. Kruhl, 1998). However, the transitions from mixed basal ⟨*a*⟩, rhomb ⟨*a*⟩, and prism ⟨*a*⟩ (type-I and II girdles) to dominantly rhomb ⟨*a*⟩ and prism ⟨*a*⟩ to purely prism ⟨*a*⟩ slip (*Y* axis maxima) are poorly constrained. To place temperature ranges on these quartz slip systems, quartz LPO opening angles (Fig. 6) along with the corresponding deformation temperatures estimated from quartz recrystallization textures from this study and from Langille et al. (2010) on samples from Mabja Dome (Fig. 2) were compiled to constrain deformation temperatures expected for the quartz LPO patterns shown in Fig. 5A. With the exception of samples AD07-17a, AD07-12b, and AD07-03 from this study, samples that exhibit dominantly basal ⟨*a*⟩, rhomb ⟨*a*⟩, and prism ⟨*a*⟩ slip (Figs. 5A and 6) have quartz BLG recrystallization suggesting deformation temperatures of ~280–400 °C. Opening angle derived temperatures from these samples fall within this temperature range. Samples which exhibit dominantly rhomb ⟨*a*⟩ and prism ⟨*a*⟩ slip along with minor basal ⟨*a*⟩ slip (Figs. 5A and 6) display quartz microstructures suggesting SGR recrystallization and opening angles indicating deformation temperatures of ~400–500 °C. Samples that exhibit dominantly prism ⟨*a*⟩ slip with minor rhomb ⟨*a*⟩ and basal ⟨*a*⟩ slip (Figs. 5A and 6) have quartz suggesting GBM recrystallization and opening angles that indicate deformation temperatures of ~500–650 °C. While temperatures of >650 °C are not recorded in this study, other studies (i.e. Lister and Dornsiepen, 1982; Mainprice et al., 1986) show that at these temperatures quartz begins to show chessboard extinction and quartz LPOs exhibit prism [*c*] slip (Fig. 5A).

4.3. Two-feldspar geothermometry

Simpson and Wintsch (1989) suggest that myrmekite replaces K-feldspar porphyroclasts in areas of high-strain. During deformation the replacement occurs adjacent to foliation surfaces (C-surfaces) facing the maximum shortening direction (S-surfaces) (Fig. 7A and B). They suggest that two-feldspar geothermometry of strain-induced myrmekite replacement in K-feldspar porphyroclasts can estimate deformation temperatures associated with an incremental shortening direction.

Sample KA-40 (Sharkha transect) contains an asymmetric K-feldspar grain with blades of albite that contain a network of vermicular quartz that extends into the interior of the grain

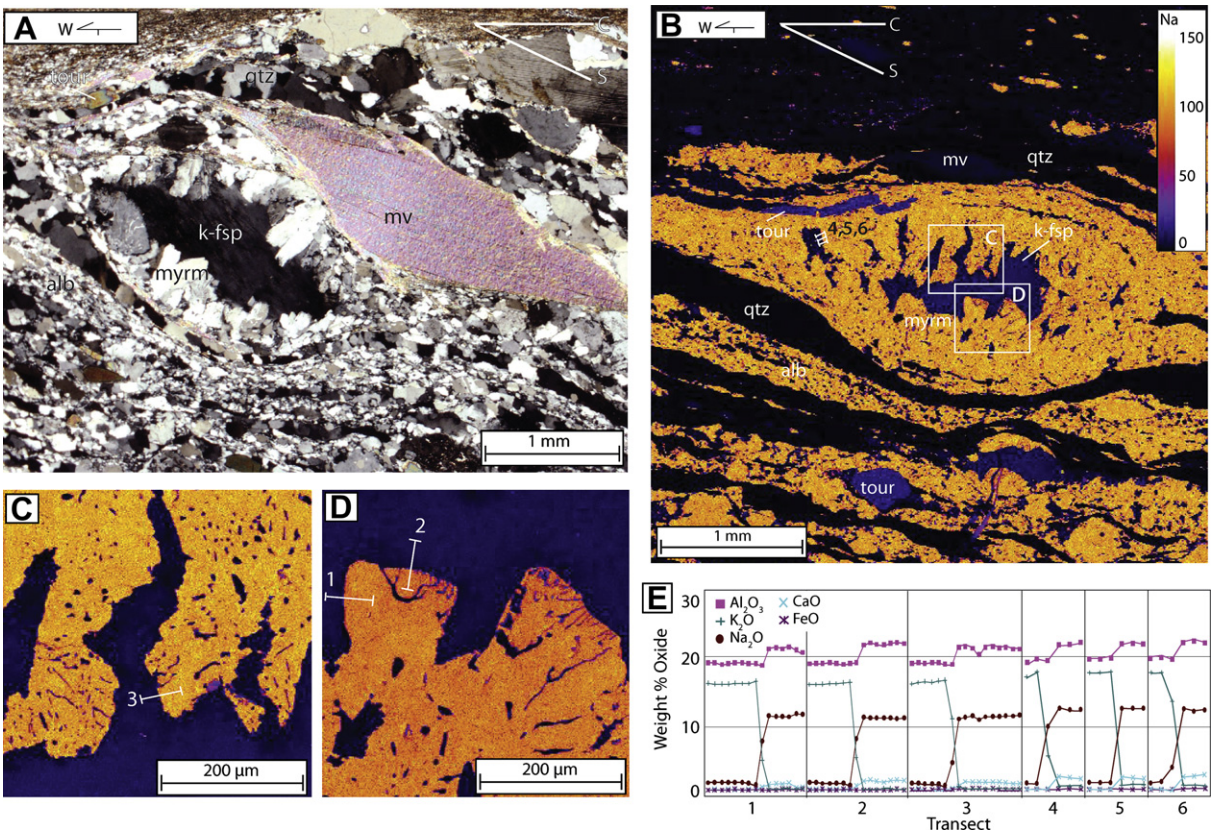

Fig. 7. (A) Asymmetric myrmekite in sample KA-40 from the Sharka transect. k-fsp, potassium feldspar; myrm, myrmekite; alb, albite; mv, muscovite; tour, tourmaline; cross polars. (B) Na compositional map of the asymmetric myrmekite cut deeper to create a second thin section of the same clast. Locations of composition transects included: 1–3 in boxes C and D and 4–6 in (B). (C) and (D) are detailed Na compositional maps of myrmekite lobes outlined in (B). Composition scale is the same as that in (B). (E) Compositional data for the six transects.

(Fig. 7A). After initial identification, a second polished thin section was made using the same billet for microprobe analysis. The myrmekite is distributed asymmetrically on the K-feldspar grain and extends ~90° from the S-surfaces. S–C fabric and mica fish confirm top-to-the-west shear sense (Fig. 7A). This strain-induced myrmekite provides a rare opportunity to quantify deformation temperatures directly associated with the development of shear sense indicators that record top-to-the-west sense of shear in the ADD.

$$T(\mathrm{K}) = \frac{\left\{7973.1 - 16910.6X_{\mathrm{ab,AF}} + 9901.9X_{\mathrm{ab,AF}}^2 + \left(0.11 - 0.22X_{\mathrm{ab,AF}} + 0.11X_{\mathrm{ab,AF}}^2\right)P\right\}}{\left\{-1.9872\ln\left(\frac{X_{\mathrm{ab,AF}}}{\alpha_{\mathrm{ab,PL}}}\right) + 6.48 - 21.58X_{\mathrm{ab,AF}} + 23.72X_{\mathrm{ab,AF}}^2 - 8.62X_{\mathrm{ab,AF}}^3\right\}} \quad (1)$$

Minimum and maximum temperatures of replacement are based on the analytical expressions of Whitney and Stormer (1977) where deformation temperature can be calculated using the equation:
where $X_{\mathrm{ab,AF}}$ is the molar fraction of albite in the K-feldspar porphyroclast, $\alpha_{\mathrm{ab,PL}}$ is the activity coefficient of albite in the myrmekite, and P (bars) is an assumed pressure. This equation is modified from the original feldspar geothermometer presented by Stormer (1975).

Compositional maps were made of portions of the myrmekite blades (Fig. 7C and D). In addition, orientation maps of portions of the myrmekite blades were created using EBSD at the University of California, Santa Barbara to test for the development of a crystal lattice and suggest that the myrmekite contains a lattice independent of the K-feldspar. Microprobe analyses were carried out on a Cameca SX-100 electron microprobe at the University of Tennessee. Na and K compositional maps of the entire grain as well as smaller areas were created to define mineral zoning and justify the locations for quantitative point analyses (Fig. 7B, C, and D). Mapping was done at 15 keV, 20 nA, and a dwell time of 0.1 s. Mineral composition analyses along six transects (Fig. 7E; Table 2) within the K-feldspar porphyroclast containing strain-induced myrmekite were conducted at 15 keV, 10 nA, and a 5 μm spot size. Activity coefficients (with an error of ± 3% propagated from the microprobe data) were calculated from electron microprobe data using the program AX (Holland and Powell, 2000) (Table 2).

4.4. Results

Samples at the top of the shear zone along the Pung Chu transect contain quartz that records BLG recrystallization (Fig. 4F) that overprints a higher temperature fabric. SGR recrystallization (Fig. 4G) within the shear zone rocks suggest an increase in deformation temperature from ~280–400 °C at the top of the shear zone to ~400–500 °C structurally deeper within the shear zone (Fig. 8A, Table 1). Feldspar porphyroclasts within samples from this transect all deform by brittle fracturing. Flame perthite is present within some albite porphyroclasts (Fig. 4G) indicating deformation temperatures of 400–500 °C. The quartz [c] axis opening angle indicates deformation temperatures of 324 ± 50 °C and 354 ± 50 °C (KA-25) at the top of the shear zone and 480 ± 50 °C (KA-02) structurally deeper in the shear zone (Fig. 6), which confirms estimates based on quartz and feldspar microstructures (Fig. 8A, Table 1). Quartz [c] and ⟨a⟩ axis LPO patterns from this transect record a range from multiple slip systems to those that are dominated by prism ⟨a⟩ slip agreeing with deformation temperatures of 280–500 °C (Fig. 6).

Within samples from the Sharkha transect, quartz experienced SGR recrystallization and feldspar porphyroclasts that deform by brittle fracture indicating deformation temperatures of 400–500 °C (Fig. 8B, Table 1). Quartz [c] and ⟨a⟩ axis LPO patterns indicate mixed slip dominated by rhomb ⟨a⟩ and prism ⟨a⟩ slip suggesting deformation temperatures of 400–500 °C (Fig. 6). Assuming 0.5 GPa, two-feldspar geothermometry (see Section 4.3) of the strain-induced myrmekite within sample KA-40 indicates that top-to-the-west shear occurred at deformation temperatures of 369–435 °C, from calculations on six compositional transects (Fig. 9). Calculations were also made assuming a pressure of 0.8 GPa and demonstrate that the calculation is relatively insensitive to changes in assumed pressure and resulted in <40 °C difference. These data were compared to temperatures derived using the Nekvasil and Burnham (1987) two-feldspar geothermometer with the program SOLVCALC (Wen and Nekvasil, 1994), which yielded temperatures within <25 °C of estimates derived from the Whitney and Stormer (1977) method (Fig. 9).

Other studies (i.e. Vernon, 1991; Hippert and Valarelli, 1998) dispute the formation of strain-induced myrmekite suggesting that there is no microstructural evidence for myrmekite replacement of K-feldspar. However, our study shows that myrmekite often protrudes into the K-feldspar at ~90° to the S-surfaces (Fig. 7A). Our estimate for deformation temperature derived from both the Whitney and Stormer (1977) and Nekvasil and Burnham (1987) models also agree with independent deformation temperatures derived from quartz and feldspar microstructures and quartz slip systems inferred from the LPO (Fig. 8B, Table 1).

Quartz experienced SGR to GBM recrystallization within samples from the Yo Ri 1 transect indicating deformation temperatures ranging from 400 to 650 °C (Fig. 8C, Table 1). Sample AD07-12b contains sillimanite cored muscovite fish and GBM recrystallization overprinted by lower temperature SGR recrystallization. Sample AD07-17a also has GBM recrystallization overprinted by lower temperature SGR recrystallization. Feldspar porphyroclasts within this transect deform mainly by brittle fracturing with minor bulging recrystallization at grain boundaries indicating temperatures of 400–650 °C (Fig. 8C, Table 1). Quartz [c] and ⟨a⟩ axis LPO patterns indicate slip dominated by rhomb ⟨a⟩ and prism ⟨a⟩ slip agreeing with deformation temperatures of 400–500 °C (Fig. 6).

Table 2
Rim compositions of K-feldspar and myrmekite.

Transect	1	2	3	4	5	6
K-feldspar						
$X_{\mathrm{ab,AF}}$	0.05	0.06	0.04	0.05	0.05	0.06
$X_{\mathrm{an,AF}}$	0	0	0	0	0	0
$X_{\mathrm{or,AF}}$	0.95	0.94	0.96	0.95	0.95	0.94
Total %	100	100	100	100	100	100
Myrmekite						
$X_{\mathrm{ab,PF}}$	0.93	0.89	0.92	0.95	0.95	0.94
$X_{\mathrm{an,PF}}$	0.06	0.1	0.04	0.04	0.04	0.05
$X_{\mathrm{or,PF}}$	0.01	0.01	0.04	0.01	0.01	0.01
Total %	100	100	100	100	100	100
$\alpha_{\mathrm{ab,PF}}$	0.92	0.89	0.92	0.95	0.95	0.94

Note: refer to Fig. 7C–E for transect locations. X_{ab}, molar fraction of albite; X_{an}, molar fraction of anorthite; X_{or}, molar fraction of orthoclase; AF, alkali feldspar; PF, plagioclase; $\alpha_{\mathrm{ab,PF}}$, activity coefficient of albite in myrmekite.

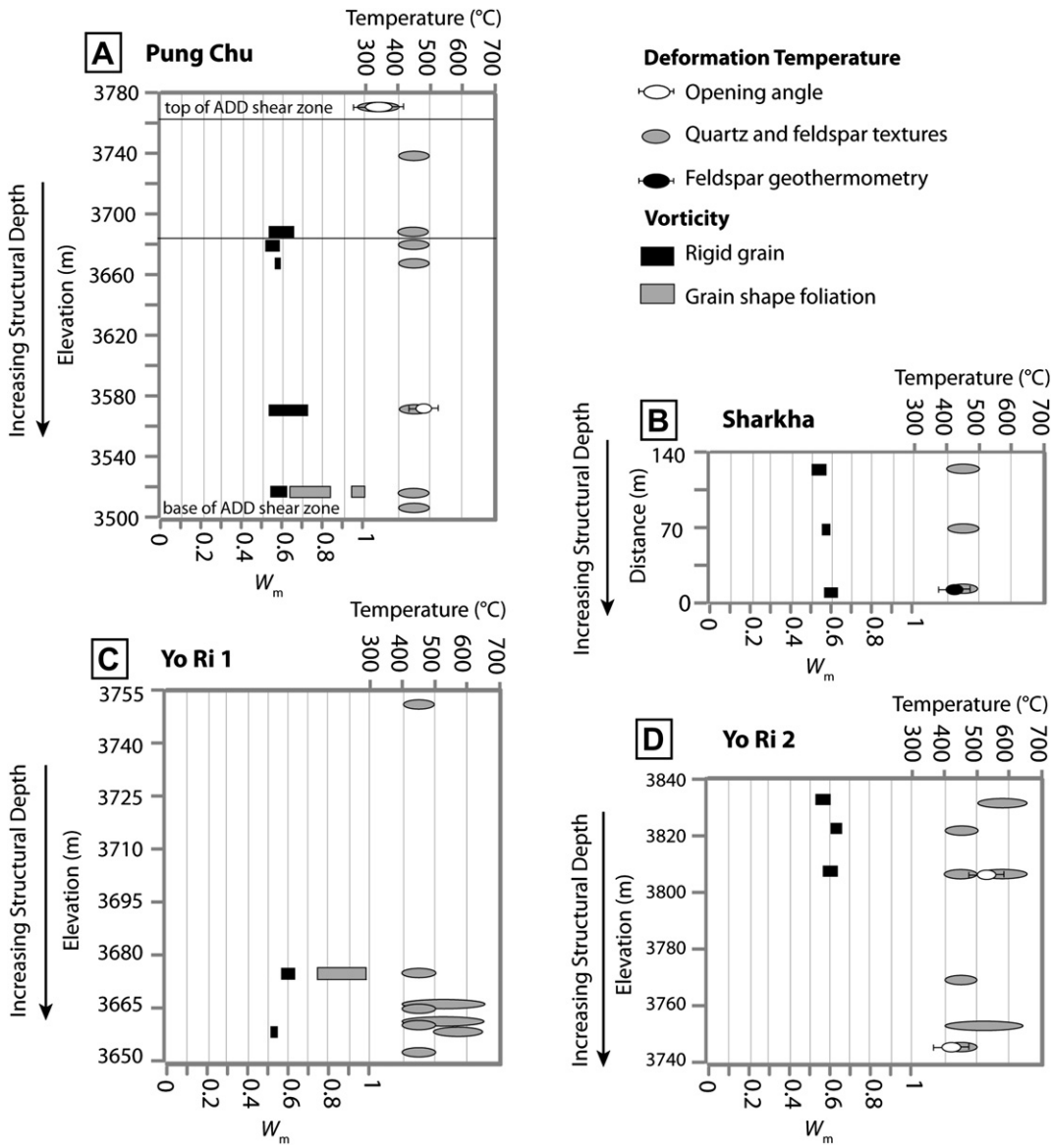

Fig. 8. Deformation temperatures and vorticity estimates for samples from the (A) Pung Chu transect, (B) Sharka transect, (C) Yo Ri 1, and (D) Yo Ri 2 transects. Multiple samples at or near the same structural depth represented as a single rectangle and/or ellipse. Vorticity and deformation temperature methods discussed in text.

Quartz experienced SGR to GBM recrystallization within samples from the Yo Ri 2 transect indicating deformation temperatures that range from 400 °C to 650 °C (Fig. 8D, Table 1). Feldspar porphyroclasts within this transect deform mainly by brittle fracturing with smaller clasts deforming plastically indicating deformation temperatures of 400–650 °C. Sample AD07-03 contains GBM recrystallization overprinted by SGR recrystallization. The quartz [*c*] axis opening angle from sample AD07-06 indicates deformation temperatures of 536 ± 50 °C and the angle from sample AD07-02 indicates temperatures of 414 ± 50 °C, both similar to those based on quartz and feldspar textures (Figs. 6 and 8D, Table 1). Quartz [*c*] and ⟨*a*⟩ axis LPO patterns from this transect exhibit mixed ⟨*a*⟩ slip dominated by prism ⟨*a*⟩ slip agreeing with deformation temperatures ranging between 400 and 650 °C (Fig. 6).

Quartz experienced SGR and GBM recrystallization within the three samples from the NRD on the eastern limb indicating deformation temperatures that range from 400 to 650 °C (Fig. 8, Table 1). Feldspar porphyroclasts from these samples deform mainly by brittle fracturing with minor BLG recrystallization also indicating temperatures between 400 and 650 °C (Tullis and Yund, 1991) (Table 1). Quartz [*c*] and ⟨*a*⟩ axis LPO patterns from MJAD-23 suggest dominantly prism ⟨*a*⟩ slip agreeing with deformation temperatures between 500 and 650 °C (Fig. 6E). These deformation temperatures overlap with those from deformed rocks along the ADD.

5. Vorticity

Vorticity analyses were conducted to quantify the relative contribution of pure and simple shear during ductile deformation and to characterize the spatial and temporal variability in flow during exhumation along the ADD. Characterizing the proportions of pure and simple shear is important because a significant contribution of pure shear indicates significant thinning and extension, and an increase in strain and extrusion rates relative to simple shear (Law et al., 2004). Kinematic vorticity number (W_k) is a measure of the relative contributions of pure ($W_k = 0$) and simple ($W_k = 1$) shear during steady-state (instantaneous) deformation. In this nonlinear relationship pure and simple shear

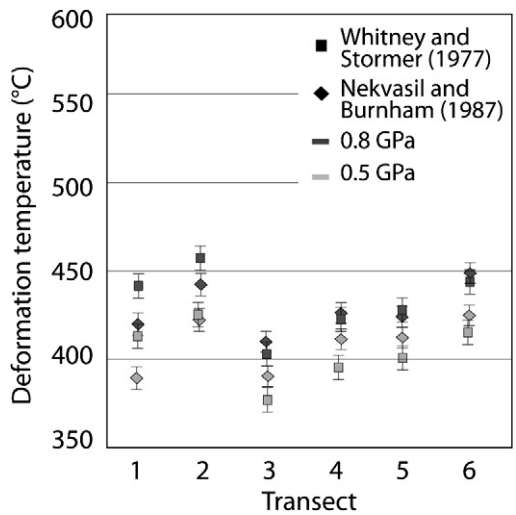

Fig. 9. Estimated deformation temperatures for all six transects through the asymmetric myrmekite. Refer to Fig. 7 for transect locations.

components are equal when $W_k = 0.71$ (Tikoff and Fossen, 1995; Law et al., 2004). The potential for spatial and temporal variability of vorticity in naturally deformed rocks (e.g. Fossen and Tikoff, 1997, 1998; Jiang, 1998) can be accounted for by using a time-averaged and assumed steady-state deformation history known as the mean kinematic vorticity number (W_m). W_m methods require that deformation progressed during plane strain conditions.

To estimate W_m, we applied two methods to thin sections cut perpendicular to the foliation and parallel to the lineation (*XZ* section); the rigid-grain technique (Passchier, 1987; Wallis et al., 1993; Jessup et al., 2007) and the quartz grain shape foliation technique (Wallis, 1995). Measurements were made directly from photomicrographs of the entire thin section taken using a high definition Nikon DS-Fi1 camera. Aspect ratio and angle data was collected on-screen using the semi-axis and angle measurement tools of the Nikon Imaging System-Elements 2.3 imaging software (Laboratory Imaging, 2007) (Fig. 10A) and saved allowing for later reference to measured grains. Grain quality was evaluated both from the photomicrographs and on the microscope. This method allows for efficient and more accurate measurement compared to standard optical measurement techniques.

5.1. Rigid-grain technique

The rigid-grain technique (Wallis et al., 1993) was applied to 19 samples and involves measuring the aspect ratio (R) of a rigid porphyroclast such as feldspar and the acute angle (θ) between the clast long axis and the macroscopic foliation (Fig. 10A). Grains above a critical aspect ratio (R_c) define a stable orientation and will exhibit a small range in θ, whereas grains below infinitely rotate and will show a larger range of θ. From R_c, vorticity can be calculated as (Passchier, 1987):

$$W_m = \left(R_c^2 - 1\right) / \left(R_c^2 + 1\right) \quad (2)$$

Plotting the shape factor (B^*), where

$$B^* = \left(M_x^2 - M_n^2\right) / \left(M_x^2 + M_n^2\right) \quad (3)$$

and M_x = long axis and M_n = short axis of a clast, versus θ on the Rigid Grain Net (RGN) is a graphical approach to calculating W_m

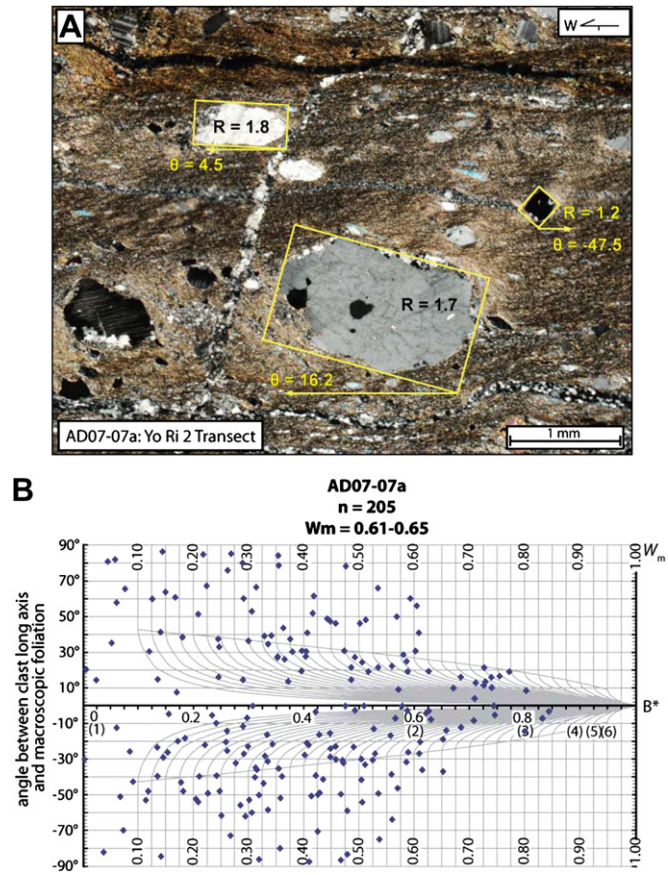

Fig. 10. (A) Example of grain axis and angle measurement. R is the aspect ratio and θ is the angle to the foliation. (B) Rigid Grain Net (RGN) of feldspar porphyroclasts corresponding to the sample in (A). n = number of grains measured. B^* is the shape factor (refer to text) and the numbers in parenthesis are aspect ratios.

(Fig. 10B) (Jessup et al., 2007). Similar to R_c, the critical shape factor B_c^* separates grains that reached a stable orientation versus those that rotated freely. W_m can be determined directly from B^* because B^* and W_m are scaled one to one.

The following criteria must be met to apply the rigid-grain technique; (1) the porphyroclasts must predate the dominant deformation fabric, (2) the porphyroclasts are internally undeformed, (3) there is no mechanical interaction between adjacent clasts or the matrix, and (4) the porphyroclasts occur within a homogeneously deformed matrix (Jessup et al., 2007). Uncertainties in vorticity values estimated using this technique can arise if; (1) recrystallization changes the aspect ratio (R) during or after deformation, (2) high-aspect ratio rigid grains in low-strain rocks have not rotated into their stable orientations, (3) rigid grains with high-aspect ratios are fractured, or (4) the sectional radii of the porphyroclast in the thin section misrepresents the actual radii (Jessup et al., 2007; Iacopini et al., 2008). To limit potential inaccuracies, grains measured showed little to no sign of plastic deformation, mechanical interaction with other grains, recrystallization, or fracturing.

5.2. Quartz grain shape foliation technique

During deformation, newly recrystallized grains (e.g. quartz) are stretched parallel to the instantaneous stretching axis (ISA) (Wallis, 1995). The maximum angle (θ) between the oblique grain shape fabric and the flow plane provides an approximate orientation of

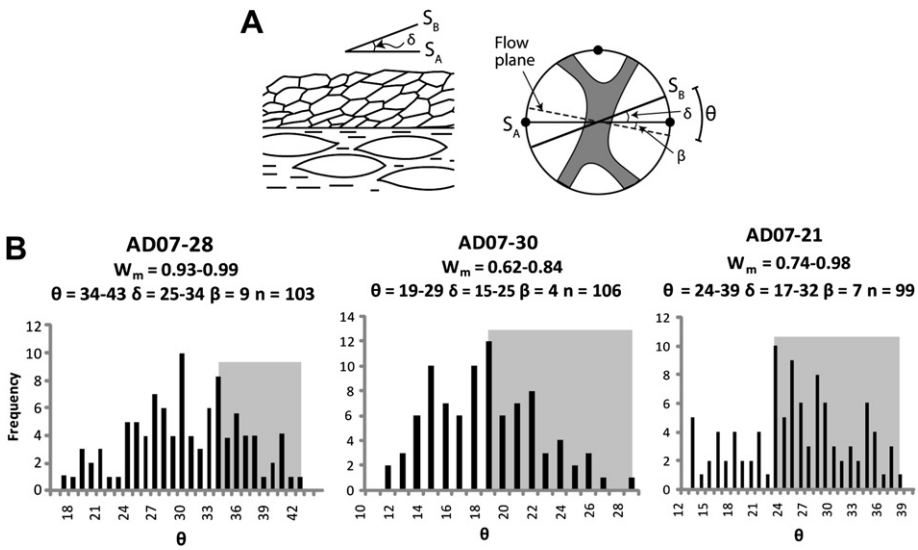

Fig. 11. (A) Schematic diagram demonstrating the relationship between the main foliation (S_A), the quartz grain shape foliation (S_B), the flow plane, and the quartz [c] axis LPO. (B) Frequency diagrams used for vorticity (W_m) estimates using the quartz grain shape foliation technique. θ = the angle between S_B and the flow plane. n = number of analyses. Shaded regions represent the range in θ used for W_m estimates.

the ISA (Wallis, 1995). The flow plane is defined as the perpendicular to the [c] axis girdle of the quartz LPO where β is the angle between the flow plane and the main foliation (S_A) (Fig. 11A) (Law, 1990; Wallis, 1995). The orientation of the ISA is related to W_m by the equation (e.g., when $\theta = 45$, $W_m = 1$; Wallis, 1995):

$$W_m = \sin 2\theta = \sin[2(\delta + \beta)] \tag{4}$$

where δ is the angle between the quartz oblique grain shape fabric (S_B) and S_A (Fig. 11A).

The long axis of the quartz grains from three samples was measured from the high-resolution mosaic image of the thin section and the flow plane was measured from the quartz LPO patterns (Fig. 6). To accurately define the ISA, θ was measured on ~100 quartz grains per sample (Fig. 11B). Application of the grain shape foliation technique requires a well-developed quartz LPO and oblique grain shape fabric to accurately define both the flow plane and the ISA, and thus θ (Wallis, 1995; Xypolias and Koukouvelas, 2001; Xypolias, 2009). Histograms were used to define the range in θ used for the W_m estimate. To accurately represent the dominant quartz fabric, the range in θ used for the W_m estimate was defined as where the frequency of θ on the histogram reaches its highest value to where it declines to a maximum measured angle (grey area in Fig. 11B).

Uncertainties in vorticity values estimated using this technique can be attributed to; (1) heterogeneity of matrix material, (2) the presence of porphyroclasts, and (3) folding—which may all deflect or influence the orientation of the quartz fabric. To limit possible inaccuracies, measurements were made from quartz fabrics that were unaffected by these interferences.

5.3. Results

From the Pung Chu transect, W_m estimates using the rigid-grain technique[1] on feldspar porphyroclasts range between 0.52 and 0.72 (49–65% pure shear) ($n = 11$). Our vorticity estimates assume plane strain deformation which is supported by the development of quartz [c] axis single girdles, type-I cross-girdles, and prism ⟨a⟩ slip patterns in the Y-direction (refer to Figs. 5 and 6) which indicate plane strain (Lister and Hobbs, 1980). Two exceptions include samples AD07-28 and AD07-30 which have ⟨a⟩ axis patterns subparallel to the lineation suggesting flattening (Fig. 6) (Lister and Hobbs, 1980; Barth et al., 2010). However, Tikoff and Fossen (1995) note that the proportion of pure shear measured in 2D on rocks that record non-plane strain is only overestimated by <0.05, which is minor compared to standard errors associated with W_m measurement. In addition, these samples yield W_m estimates consistent with the other samples in this study suggesting that these measurements are reliable (Fig. 8A, Table 1). W_m estimates using the quartz grain shape foliation technique range from 0.62 to 0.99 (1–57% pure shear) ($n = 2$) within samples from the Pung Chu transect, suggesting dominantly simple shear to sub-equal amounts of pure and simple shear (Fig. 8A, Table 1).

W_m estimates using the rigid-grain technique on rigid feldspar porphyroclasts were applied to three samples from the Sharkha transect and yield estimates that range from 0.50 to 0.61 (58–66% pure shear) (Fig. 8B, Table 1), similar to those in the Pung Chu transect. The rigid-grain technique was applied to feldspar in two samples from the Yo Ri 1 transect and yielded values of 0.52–0.64 (55–64% pure shear) suggesting a dominant pure shear component. These estimates are similar to those from the other transects. The quartz grain shape foliation technique was applied to AD07-21 from the Yo Ri 1 transect and yielded values of 0.74–0.98 (1–44% pure shear), suggesting a large simple shear component (Fig. 8C, Table 1). The rigid-grain technique was applied to feldspar in three samples from the Yo Ri 2 transect and yielded W_m estimates ranging from 0.53 to 0.65 (54–64% pure shear) suggesting a large pure shear component (Fig. 8D; Table 1).

6. Shortening and extension

The strain ratio (R_{xz}) can be calculated from the following equation which utilizes the angular relationships between the quartz oblique grain shape fabrics and quartz [c] axis fabrics (Passchier, 1988; Xypolias, 2009):

$$R_{xz} = \frac{1 - \tan\theta \tan\beta}{\tan^2\beta + \tan\theta \tan\beta} \tag{5}$$

[1] Additional Rigid Grain Net plots can be found in the Data Repository.

where

$$\tan\theta = \cot[2(\beta+\delta)] = \sqrt{1-W_m^2}/W_m \quad (6)$$

and β is the angle between the flow plane and S_A as measured from the quartz [c] axis fabric and δ is the angle between the quartz oblique fabric (S_B) and the main foliation (S_A) (Fig. 11A). This equation was applied to three samples from the ADD and yields R_{xz} values of 6.4–27 (Table 1).

Using our W_m (1–44% pure shear, from the quartz grain shape fabric technique) and R_{xz} estimates (6.7–24) from sample AD07-21 (our only quartz W_m estimate with evidence for plane strain deformation), percent shortening and down-dip extension were estimated by calculating the shortening perpendicular to the flow plane (S) (stretch parallel to the flow plane is defined as S^{-1}) using the following equation (Wallis et al., 1993):

$$S = \left\{0.5\left(1-W_m^2\right)^{0.5}\left[\left(R_{xz}+R_{xz}^{-1}+\frac{2\left(1+W_m^2\right)}{\left(1-W_m^2\right)}\right)^{0.5} + \left(R_{xz}+R_{xz}^{-1}-2\right)^{0.5}\right]^{-1}\right\} \quad (7)$$

Our data show that this sample experienced between 36–50% shortening and 57–99% down-dip extension at the time that our vorticity estimates were recorded in the deformed quartz at temperatures of 400–500 °C (deformation temperature estimate for sample AD07-21).

7. Discussion

7.1. Implications for the Ama Drime and Nyönno Ri detachments

The ADM records anatectic melting in the core of the range during the onset of orogen-parallel extension (Cottle et al., 2009a). Exhumation (2.2 ± 0.2 mm/yr) was accommodated by two shear zones (ADD and NRD) that currently dip in opposite direction away from the core of the range (Cottle et al., 2009a). Shear zone nucleation occurred at high-temperatures as a distributed shear zone that was progressively overprinted by deformation mechanisms that were active at decreasing temperature and varying strain rates (Fig. 12). Pseudotachylite records high-strain events that punctuated the exhumation history. Qualitative evidence for this range in deformation conditions that occurred at high temperature and presumably an earlier portion of the history is taken from footwall rocks whereas brittle detachments that occur within the section record the final stages of exhumation. Mylonitic samples from the ADD and NRD provide an opportunity to quantify the kinematic evolution of solid-state fabric development that link early and late stages of this exhumation history.

Mean kinematic vorticity estimates from rocks within the ADD range between 0.50 and 0.72 (49–66% pure shear) using the rigid-grain technique (n = 19) and 0.62–0.99 (1–57% pure shear) using the oblique quartz grain shape foliation technique (n = 3). Vorticity estimates derived from quartz fabrics record a higher component of simple shear than estimates derived from rigid porphyroclasts.

Assuming quartz is more sensitive to late stage changes in deformation than the rigid porphyroclasts, W_m estimates derived from the quartz fabrics can be interpreted as recording the last increment of ductile deformation (Wallis, 1995; Xypolias, 2009). This interpretation was suggested for Rongbuk valley where quartz fabrics yield higher W_m estimates than those obtained using rigid porphyroclasts (Law et al., 2004). Johnson et al. (2009a,b) propose that increased mica content results in decoupling between the porphyroclast and matrix interface, which can potentially overestimate the pure shear component when rigid porphyroclasts are used for W_m estimates. Because our W_m estimates are consistent between samples that contain a range in composition and mica

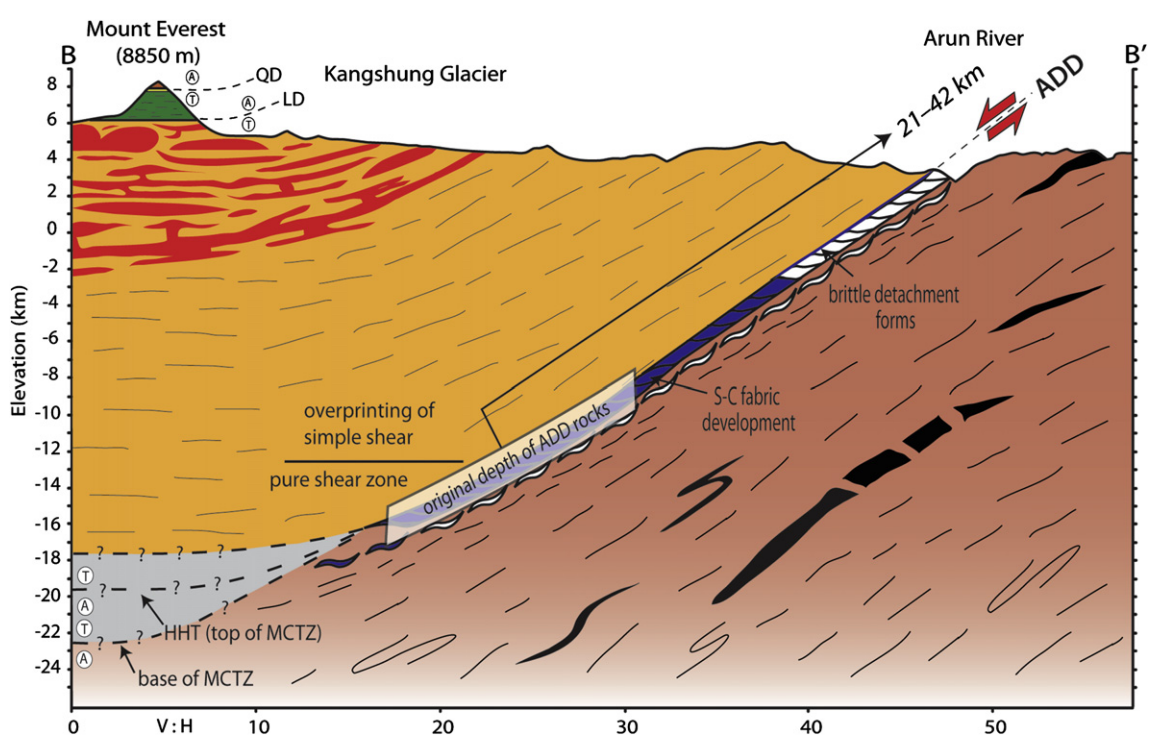

Fig. 12. Simplified geologic cross section through Mt. Everest and the Ama Drime Massif with a schematic diagram overlay that depicts the kinematic evolution of the Ama Drime detachment (ADD) assuming a geothermal gradient of 25–35 °C/km. Refer to Fig. 2 for cross section location and legend. Blue on the shear zone demonstrates active systems present as the rocks were exhumed and narrowed into the ~300-m-thick shear zone. Shear zone thickness not to scale. Other possible depths for the deepest position of the ADD are dashed. QD, Qomalangma detachment; LD, Lhotse detachment; HHT, High Himalayan thrust.

content (i.e. marble, quartzite, leucogranite, etc.), we suggest that decoupling was either minimal or if present, the decoupling resulted in an error that was independent of mica content. In addition to our vorticity estimates, the asymmetry or lack of asymmetry of quartz LPO patterns (Fig. 6) suggests that some samples record noncoaxial deformation (e.g. KA-25 and AD07-04) while others suggest coaxial deformation (e.g. AD07-12b, AD07-17a, AD07-03). As mentioned earlier, samples AD07-17a, AD07-12b, and AD07-03 contain quartz GBM recrystallization overprinted by SGR recrystallization suggesting that earlier pure shear dominated flow is associated with GBM (coaxial quartz LPO patterns and rigid-grain technique vorticity estimates) at higher temperatures and was overprinted by noncoaxial flow (quartz grain shape foliation vorticity estimates) at lower temperatures.

We propose that the rigid-grain technique (49–66% pure shear) records an early part of the exhumation history when deformation transitioned from high-temperature distributed shear to mylonite development (Fig. 12). This was followed by W_m estimates from quartz fabrics (1–57% pure shear) that record a later part of the exhumation history as these rocks were exhumed (Fig. 12). These data indicate a spatial and temporal variation in deformation that progressed from dominantly pure shear to dominantly simple shear deformation during exhumation between ~400 and 650 °C. Our data from sample AD07-21 indicates that the rocks exposed within the ADD experienced 36–50% shortening and 57–99% down-dip extension at the time that the vorticity estimates were recorded in the deformed quartz. Previous estimates using original quartz grain aspect ratios and telescoped isograds yielded 10–30% shortening and 10–40% down-dip extension within the GHS near the STDS in the Mabja Dome and the Everest region (Law et al., 2004; Langille et al., 2010). This implies that the rocks exposed within the ADD experienced a significantly larger amount of strain during the later increments of ductile deformation than estimated from the GHS in the footwall of the STDS.

Deformation temperatures derived from asymmetric quartz [*c*] axis LPO opening angles and two-feldspar thermometry of asymmetric myrmekite that are directly related to top-to-the-west shear (369–587 °C) were used to estimate the amount of top-to-the-west displacement on the ADD. Assuming a geothermal gradient of ~25–35 °C/km, our deformation temperature estimates suggest that the rocks exposed within the ADD shear zone were exhumed from a minimum depth of 11–21 km (Fig. 12). Projecting this depth below the current surface expression of the ADD using a constant dip of ~30° for the ADD (based on structural data from Jessup et al., 2008a; Fig. 2) yields a minimum of ~21–42 km of down-dip displacement (Fig. 12), similar to other estimates of ~30 km (Kali et al., 2010). Uncertainties are associated with the poorly constrained geothermal gradient and our assumed dip for the detachment. Estimates of deformation temperatures (400–650 °C) experienced by rocks exposed within the NRD (Fig. 6, Table 1) indicate that it exhumed footwall rocks from similar depths as the ADD. The Gurla Mandhata core complex, ~650 km west of the ADM, is another feature that was exhumed during orogen-parallel extension. The core complex is bound on the west by the Gurla Mandhata-Humla extensional fault system that records 35–66 km of top-to-the-west displacement during extension after 15 Ma (Murphy, 2007; Murphy et al., 2002), similar to our displacement estimate for the ADD.

7.2. Comparison with the North Himalayan gneiss domes

Although the ADM is located just south of two of the North Himalayan gneiss domes, the Lhagoi Kangri and Mabja domes (Figs. 1 and 2A), our data suggests that these are very different types of migmatite-cored domes. North Himalayan gneiss domes expose middle crustal rocks belonging to an originally ~35-km-thick mid-crustal channel composed of the GHS (e.g. Burg and Chen, 1984; Chen et al., 1990; Lee et al., 2000, 2002, 2004, 2006; Zhang et al., 2004; Aoya et al., 2005, 2006; Quigley et al., 2006, 2008; Lee and Whitehouse, 2007). W_m studies of the GHS (Grasemann et al., 1999; Law et al., 2004; Carosi et al., 2006, 2007; Jessup et al., 2006; Larson and Godin, 2009) suggest that the low-viscosity mid-channel deformed by general shear with an increasing component of pure shear towards the center. Langille et al. (2010) demonstrated that mid-crustal rocks exposed within the Mabja dome preserve mixed top-to-the-north and top-to-the-south shear at the top of the channel and top-to-the-south shear toward the bottom, an increasing pure shear component with structural depth, and increasing deformation temperatures towards the middle of the dome, patterns consistent with those predicted for the deformed mid-crustal channel. Lee et al. (2006) and Lee and Whitehouse (2007) suggest that these deformational patterns were developed between ~16 and 35 Ma, and correlate closely to ages estimated for metamorphism and anatexis of the GHS (Burg and Chen, 1984; Pognante and Benna, 1993; Simpson et al., 2000; Viskupic et al., 2005; Cottle et al., 2009b). Data from the Mabja and the Kangmar domes (Lee et al., 2000) suggest that the rocks exposed within the North Himalayan gneiss domes originated from within the mid-crustal channel and were later brought to the surface through thrust faulting along the Gyirong-Kangmar thrust fault during the middle Miocene (Burg and Chen, 1984; Burg et al., 1987; Lee et al., 2000).

Structural and geochronologic data (i.e. Liu et al., 2007; Zhang and Guo, 2007; Jessup et al., 2008a; Cottle et al., 2009a; This study) suggest that the kinematic, metamorphic, and exhumation history of the ADM differs from that of the North Himalayan gneiss domes. In contrast to the rocks exposed within Mabja Dome that record a spatial transition from dominantly simple shear to dominantly pure shear deformation that developed simultaneously with increasing structural depth across the dome, the rocks exposed within the ADD record a temporal transition with an early phase of movement that was dominated by pure shear deformation that is overprinted by predominantly simple shear deformation during the later stages of the exhumation history on the shear zone (Fig. 12). In addition, the rocks exposed within the ADD were deformed at temperatures ranging between ~400 and 650 °C and are exposed within a ~300-m-thick shear zone. In contrast, the rocks exposed within the Mabja Dome record deformation temperatures increasing from ~450 °C to >700 °C and are exposed within a 13-km-thick zone. Kinematic indicators within the ADD and NRD indicate opposite sense of shear on either side of the ADM that record orogen-parallel extension. Mabja is dominated by top-to-the-north shear sense that transitions to top-to-the-south shear sense with increasing structural depth related to south-directed flow. $^{40}Ar/^{39}Ar$ ages for muscovite and biotite from the NRD (Zhang and Guo, 2007) and U–Th–Pb ages from the ADM (Liu et al., 2007; Cottle et al., 2009a) suggest that east–west extension initiated at ~13 Ma, which post-dates south-directed flow recorded in the North Himalayan gneiss domes by ~3 Ma. Based on these characteristics we propose that the structural and kinematic evolution of the ADM is more closely related to metamorphic domes developed during orogen-parallel extension, such as the Gurla Mandhata core complex (Murphy et al., 2002) and Leo Pargil dome (Theide et al., 2006), rather than the North Himalayan gneiss domes.

7.3. Exhumation of the Ama Drime Massif

Borghi et al. (2003) projected the MCTZ along the western side of the ADM while others (Lombardo and Rolfo, 2000; Groppo et al., 2007; Liu et al., 2007) projected the MCTZ around the ADM. Several

possibilities exist for the structural positions juxtaposed by the ADD. Lombardo and Rolfo (2000) interpret the ADM orthogneiss to correspond to the Num orthogneiss (lower GHS) whereas the grt + bt + sill gneiss in the hanging wall of the ADD is equivalent to the Barun Gneiss (upper GHS) of the Sedua-Makalu section. Based on this, they propose that the Kharta section is structurally lower relative to the MCTZ exposed in the Sedua-Makalu section (HHT of Goscombe et al., 2006). The protolith age for the Ama Drime orthogneiss is equivalent to Proterozoic gneisses in the foreland (e.g. Ulleri orthogneiss) (Goscombe et al., 2006; Searle et al., 2008; Cottle et al., 2009a).

The map relationships between the ADD, the HHT (top of the MCTZ), and STDS are depicted on a cross section from the center of the ADM to the Khumbu glacier (Fig. 12). We project the ADD ~10 km further south than our southern most mapped contacts into the border region between Tibet and Nepal to construct a cross section that is perpendicular to the ADD and that passes through a known location of the Qomolangma detachment (QD). This southern projection of the ADD is balanced by structural data from the footwall and hanging wall of the NRD from Burchfiel et al. (1992) that indicates that it extends to at least this position on the southern portion of the eastern side of the ADM (Fig. 2). The QD exposed on the summit of Mount Everest dips NNE and juxtaposes TSS in the hanging wall with the Yellow band in the uppermost section of the Everest Series schist and calc-silicate in the footwall (Burchfiel et al., 1992; Searle et al., 2003; Jessup et al., 2006; Jessup et al., 2008b). The base of the Everest Series is defined by the NE-dipping Lhotse detachment (LD) (Searle, 1999). Using the structural distance between the QD and the top of the MCTZ (HHT), the GHS between the STDS and the MCTZ is estimated to be ~28-km-thick below the QD on the summit of Mount Everest (Searle et al., 2006).

Using an average dip of 30°, the ADD can be projected from the surface to deeper structural positions, through a minimum depth of ~11–21 km from our estimated deformation temperatures, where it presumably shallows out beneath the summit of Mount Everest. Based on these data we propose that the ADD might sole into the HHT or a deeper structural position such as the base of the MCTZ or some other (lithologic, stratigraphic, or structural) boundary that is not exposed in the foreland (Fig. 12). Assuming that the orientation for this contact was originally north dipping then it was potentially rotated to its current orientation and reactivated as the ADD to accommodate exhumation of the ADM.

We propose that prior to the onset of orogen-parallel extension the crustal profile of the Everest area included a 28-km-thick section of GHS. The section was juxtaposed with the TSS at the top by top-to-the-north displacement on the STDS and granulite facies rocks at the bottom by top-to-the-south displacement on the MCTZ (Searle et al., 2006). Rocks that are currently exposed in the central section of the ADM (750 °C and 0.7–0.8 GPa) were located at an unknown structural position between the upper GHS and the LHS. Here they experienced muscovite dehydration melting (11–13 Ma) in a kinematic setting that was dominated by orogen-parallel extension.

Exhumation of footwall rocks of the NRD by 10–13 Ma was kinematically linked to extension in the interior of the Tibetan Plateau (Zhang and Guo, 2007; Kali et al., 2010). $^{40}Ar/^{39}Ar$ muscovite and biotite ages suggest that exhumation on the NRD (10–13 Ma) began prior to the ADD (6–10 Ma). One possible interpretation is that back-rotation of the NRD footwall towards the west during initial exhumation of the ADM resulted in a west-dipping lithologic or structural boundary. This weakness was reactivated during top-to-the-west shearing that produced at least 21–42 km of displacement along the portion between the Yo Ri and Pung Chu gorges. Deformed leucogranite dikes and undeformed dikes in the NRD that crosscut the main shear zone fabric indicate that ductile movement on the NRD ended by ~11 Ma (Kali et al., 2010). Displacement on the NRD and ADD decreases towards the north where it is minimal at the north-plunging nose (Kali et al., 2010). Not only does this indicate that the southernmost transects record the deepest record of the fault in our study area, but also that the Ama Drime orthogneiss exposed between these represents the deepest structural position of the massif.

8. Conclusions

New detailed microstructural and kinematic analyses, estimates of deformation temperatures, and vorticity analyses conducted on rocks from the western limb of the Ama Drime Massif suggests that these rocks record top-to-the-west shear sense between ~400 and 650 °C. Mean kinematic vorticity estimates from within this temperature interval record an earlier pure shear dominated flow (49–66% pure shear, rigid-grain technique) overprinted by a later high-strain, simple shear (1–57% pure shear, quartz fabrics) dominated flow during the later increments of ductile deformation. Our estimated deformation temperatures recorded during top-to-the-west shear are combined with an assumed dip for the detachment of 30° to create a minimum estimate of 21–42 km of displacement for the Ama Drime detachment. Data from the eastern limb of the Ama Drime Massif indicate that the Nyönno Ri detachment may have experienced a similar magnitude of displacement during exhumation of the Ama Drime Massif. We propose that exhumation of the massif began during the initiation of orogen-parallel extension in the Dinggyê graben. Back-rotation of the footwall block resulted in a west-dipping footwall block. During back-rotation, a weakness in the footwall block was reactivated to accommodate top-to-the-west shear along the ADD during orogen-parallel extension.

Acknowledgments

We thank C. Passchier, P. Xypolias, and J. Lee whose detailed reviews strengthened a previous version of this manuscript. L. Duncan and D. Breecker provided field assistance. We thank A. Patchen at the University of Tennessee for assistance with the microprobe. We thank Sonam Wangdu for logistics in Tibet during four expeditions to the Ama Drime and Kharta valley. M. Smith made initial microstructural analyses as part of her undergraduate project. Funding was provided by grants to M. Jessup from the American Alpine Club, Sigma Xi, and a 2010 Fellowship from Virginia Tech which provided funding for the initial portions of the project. Funding was also provided by the Research and Exploration grant (NG-CRE-8494-08) from the National Geographic Society to M. Jessup and the National Science Foundation grant (EAR-0911561) to M. Jessup and J. Cottle.

Appendix. Supplementary data

Supplementary data associated with this article can be found, in the online version, at doi:10.1016/j.jsg.2010.04.005.

References

Aoya, M., Wallis, S.R., Terada, K., Lee, J., Kawakami, T., Wang, Y., Heizler, M., 2005. North–south extension in the Tibetan crust triggered by granite emplacement. Geology 33, 853–856.

Aoya, M., Wallis, S.R., Kawakami, T., Lee, J., Wang, Y., Maeda, H., 2006. The Malashan gneiss dome in south Tibet: comparative study with the Kangmar dome with special reference to kinematics of deformation and origin of associated granites. In: Law, R.D., Searle, M.P., Godin, L. (Eds.), Channel Flow, Ductile Extrusion and Exhumation in Continental Collision Zones. Geological Society, London, Special Publication, vol. 268, pp. 471–495.

Armijo, R., Tapponnier, P., Mercier, J., Han, T., 1986. Quaternary extension in southern Tibet: field observations and tectonic implications. Journal of Geophysical Research 91, 13803–13872.

Barth, N.C., Hacker, B.R., Seward, G.G.E., Walsh, E.O., Young, D., Johnston, S., 2010. Strain within the ultrahigh-pressure western Gneiss region of Norway recorded by quartz CPOs. In: Law, R., Butler, R., Holdsworth, R., Krabbendam, M., Strachan, R. (Eds.), Continental Tectonics and Mountain Building: The Legacy of Peach and Horne. Geological Society, London, Special Publication.

Borghi, A., Castelli, D., Lombardo, B., Visoná, D., 2003. Thermal and baric evolution of garnet granulites from the Kharta region of S Tibet, E Himalaya. European Journal of Mineralogy 15, 401–418.

Brookfield, M.E., 1993. The Himalayan passive margin from Precambrian to Cretaceous. Sedimentary Geology 84, 1–35.

Burchfiel, B.C., Chen, Z., Hodges, K.V., Yiping, L., Royden, L.H., Deng, C., Xu, J., 1992. The South Tibetan detachment system, Himalayan orogen: extension contemporaneous with and parallel to shortening in a collisional mountain belt. In: Geological Society, America, Special Paper, vol. 269, 41 p.

Burg, J.P., Chen, J.M., 1984. Tectonics and structural zonation of southern Tibet, China. Nature 311, 219–223.

Burg, J.P., Leyreloup, A., Girardeau, J., Chen, G.M., 1987. Structure and metamorphism of a tectonically thickened continental crust: the Yalu Tsangpo suture zone (Tibet). Royal Society of London Philosophical Transactions 321, 67–86.

Carosi, R., Montomoli, C., Rubatto, D., Visoná, D., 2006. Normal-sense shear zones in the core of the Higher Himalayan Crystallines (Bhutan Himalaya); evidence for extrusion? In: Law, R.D., Searle, M.P., Godin, L. (Eds.), Channel flow, Ductile Extrusion and Exhumation in Continental Collision Zones. Geological Society, London, Special Publication, vol. 268, pp. 425–444.

Carosi, R., Montomoli, C., Visoná, D., 2007. A structural transect in the Lower Dolpo: insights on the tectonic evolution of Western Nepal. Journal of Asian Earth Sciences 29, 407–442.

Catlos, E.J., Harrison, T.M., Manning, C.E., Grove, S.M., Hubbard, M.S., Upreti, B.N., 2002. Records of the evolution of the Himalayan orogen from in-situ Th–Pb ion microprobe dating of monazite: eastern Nepal and western Garhwal. Journal of Asian Earth Sciences 20, 459–479.

Chen, Z., Liu, Y., Hodges, K.V., Burchfiel, B.C., Royden, L.H., Deng, C., 1990. The Kangmar Dome: a metamorphic core complex in southern Xizang (Tibet). Science 250, 1552–1556.

Cottle, J.M., Jessup, M.J., Newell, M.J., Searle, M.P., Law, R.D., Horstwood, M., 2007. Structural insights into the early stages of exhumation along an orogen-scale detachment: the South Tibetan Detachment system, Dzakaa Chu section, eastern Himalaya. Journal of Structural Geology 29, 1781–1797.

Cottle, J.M., Jessup, M.J., Newell, D.L., Horstwood, S.A., Noble, S.R., Parrish, R.R., Waters, D.J., Searle, M.P., 2009a. Geochronology of granulitized eclogite from the Ama Drime Massif: implications for the tectonic evolution of the South Tibetan Himalaya. Tectonics 28, 1–25.

Cottle, J.M., Searle, M.P., Horstwood, M.S.A., Waters, D.J., 2009b. Timing of Mid-crustal metamorphism, melting and deformation in the Mt. Everest region of southern Tibet revealed by U(–Th)–Pb geochronology. Journal of Geology 117, 643–664.

Dewane, T.J., Stockli, D.F., Hager, C., Taylor, M., Ding, L., Lee, J., 2006. Timing of Cenozoic E–W extension in Tangra Yum Co rift, central Tibet. Journal of Asian Earth Sciences 26, 133.

Fitz Gerald, J.D., Stünitz, H., 1993. Deformation of granitoids at low metamorphic grades. I: reactions and grain size reduction. Tectonophysics 221, 269–297.

Fossen, H., Tikoff, B., 1997. Forward modeling of non-steady-state deformations and the 'minimum strain path'. Journal of Structural Geology 19, 987–996.

Fossen, H., Tikoff, B., 1998. Forward modeling of non-steady-state deformations and the 'minimum strain path': reply. Journal of Structural Geology 20, 979–981.

Gaetani, M., Garzanti, E., 1991. Multicyclic history of the northern India continental margin (northwestern Himalaya). American Association of Petroleum of Geologists Bulletin 75, 1427–1446.

Gansser, A., 1964. Geology of the Himalayas. Wiley-Interscience, London.

Garzanti, E., 1999. Stratigraphy and sedimentary history of the Nepal Tethys Himalaya passive margin. Journal of Asian Earth Sciences 17, 805–827.

Goscombe, B., Gray, D., Hand, M., 2006. Crustal architecture of the Himalayan metamorphic front in eastern Nepal. Gondwana Research 10, 232–255.

Grasemann, B., Fritz, H., Vannay, J.-C., 1999. Quantitative kinematic flow analysis from the Main Central Thrust Zone (NW-Himalaya, India): implications for a decelerating strain path and the extrusion of orogenic wedges. Journal of Structural Geology 21, 837–853.

Groppo, C., Lombardo, B., Rolfo, F., Pertusanti, P., 2007. Clockwise exhumation path of granulitized eclogites from the Ama Drime range (Eastern Himalayas). Journal of Metamorphic Geology 25, 51–75.

Grujic, D., 2006. Channel flow and continental collision tectonics; an overview. In: Law, R.D., Searle, M.P., Godin, L. (Eds.), Channel Flow, Ductile Extrusion and Exhumation in Continental Collision Zones. Geological Society, London, Special Publication, vol. 268, pp. 25–37.

Grujic, D., Hollister, L.S., Parrish, R.R., 2002. Himalayan metamorphic sequence as an orogenic channel: insight from Bhutan. Earth and Planetary Letters 198, 177–191.

Grujic, D., Martin, C., Davidson, C., Hollister, L.S., Kuendig, R., Pavlis, T.L., Schmid, S.M., 1996. Ductile extrusion of the Higher Himalayan Crystalline in Bhutan; evidence from quartz microfabrics. Tectonophysics 260, 21–43.

Guillot, S., Mahéo, G., deSigoyer, J., Hattori, K.H., Pêcher, A., 2008. Tethyan and Indian subduction viewed from the Himalayan high- to ultrahigh-pressure metamorphic rocks. Tectonophysics 451, 225–241.

Hager, C., Stockli, D.F., Dewane, T.J., Ding, L., 2006. Episodic Mio-Pliocene rifting in south-central Tibet. Thermochronometric constraints from the Xainza rift. Eos (Transactions, American Geophysical Union) 87, T34C-02.

Hippert, J.F., Valarelli, J.V., 1998. Myrmekite: constraints on the available models and a new hypothesis for its formation. European Journal of Mineralogy 10, 317–331.

Hirth, G., Teyssier, C., Dunlap, J., 2001. An evaluation of quartzite flow laws based on comparisons between experimentally and naturally deformed rocks. International Journal of Earth Sciences 90, 77–87.

Hirth, G., Tullis, J., 1992. Dislocation creep regimes in quartz aggregates. Journal of Structural Geology 14, 145–159.

Hodges, K.V., 2000. Tectonics of the Himalaya and southern Tibet from two perspectives. Geological Society of America Bulletin 112, 324–350.

Hodges, K.V., Hurtado, J.M., Whipple, K.X., 2001. Southward extrusion of Tibetan crust and its effect on Himalayan tectonics. Tectonics 20, 799–809.

Hodges, K.V., Parrish, R., Housh, T., Lux, D., Burchfiel, B., Royden, L., Chen, Z., 1992. Simultaneous Miocene extension and shortening in the Himalayan orogen. Science 258, 1466–1470.

Holland, T. J. B. & Powell, R., 2000. AX: A program to calculate activities of mineral end members from chemical analyses (usually determined by electron microprobe).

Hubbard, M.S., Harrison, T.M., 1989. $^{40}Ar/^{39}Ar$ age constrains on deformation and metamorphism in the Main Central Thrust Zone and Tibetanslab, eastern Nepal Himalaya. Tectonics 8, 865–880.

Iacopini, D., Carosi, R., Montomoli, C., Passchier, C.W., 2008. Strain analysis and vorticity of flow in the Northern Sardinian Variscan Belt: recognition of a partitioned oblique deformation event. Tectonophysics 446, 77–96.

Jessell, M.W., 1987. Grain-boundary migration microstructures in a naturally deformed quartzite. Journal of Structural Geology 9, 1007–1014.

Jessup, M., Cottle, J. Progression from south-directed extrusion to orogen-parallel extension in the southern margin of the Tibetan Plateau, Mount Everest region, Tibet. Journal of Geology, in press.

Jessup, M.J., Law, R.D., Frassi, C., 2007. The rigid grain net (RGN): an alternative method for estimating mean kinematic vorticity number (W_m). Journal of Structural Geology 29, 411–421.

Jessup, M.J., Law, R.D., Searle, M.P., Hubbard, M.S., 2006. Structural evolution and vorticity of flow during extrusion and exhumation of the Greater Himalayan Slab, Mount Everest Massif, Tibet/Nepal: implications for orogen-scale flow partitioning. In: Law, R.D., Searle, M.P., Godin, L. (Eds.), Channel Flow, Ductile Extrusion and Exhumation in Continental Collision Zones. Geological Society, London, Special Publication, vol. 268, pp. 379–413.

Jessup, M., Newell, D.L., Cottle, J.M., Berger, A., Spotila, J., 2008a. Orogen-parallel extension and exhumation enhanced by denudation in the trans-Himalayan Arun River gorge, Ama Drime Massif, Tibet–Nepal. Geology 36, 587–590.

Jessup, M.J., Cottle, J.M., Searle, M.P., Law, R.D., Newell, D.L., Tracy, R.J., Waters, D.J., 2008b. P-T-t-D paths of Everest Series schist, Nepal. Journal of Metamorphic Geology 26, 717–739.

Jessup, M., Cottle, J.M., Newell, D., Berger, A., Spotila, J., 2008c. Exhumation of the Trans-Himalayan Ama Drime Massif: implications for orogen-parallel mid-crustal flow and Exhumation on the Southern Margin of the Tibetan Plateau. In: Joint Meeting of the Geological Society of America.

Jiang, D., 1998. Forward modeling of non-steady-state deformations and the 'minimum strain path': discussion. Journal of Structural Geology 20, 975–977.

Johnson, S., Lenferink, H., Price, N., Marsh, J., Koons, P., West, D., Beane, R., 2009a. Clast-based kinematic vorticity gauges: The effect of slip at matrix/clast interfaces. Journal of Strucural Geology 31, 1322–1339.

Johnson, S., Lenferink, H., Marsh, J., Price, N., Koons, P., West, D., 2009b. Kinematic vorticity analysis and evolving strength of mylonitic shear zones: new data and numerical results. Geology 37, 1075–1078.

Kali, E., Leloup, P.H., Arnaud, N., Mahéo, G., Liu, D., Boutonnet, E., VanderWoerd, J., Xiaohan, L., Liu-Zeng, J., Haibing, L., 2010. Exhumation history of the deepest central Himalayan rocks (Ama Drime range): key P-T-D-t constraints on orogenic models. Tectonics 29, 1–31.

Kapp, P., Guynn, J., 2004. Indian punch rifts Tibet. Geology 32, 993–996.

Kruhl, J.H., 1998. Reply: prism- and basal-plane parallel subgrain boundaries in quartz: a microstructural geothermometer. Journal of Metamorphic Petrology 16, 142–146.

Langille, J., Lee, J., Hacker, B., Seward, G., 2010. Middle crustal ductile deformation patterns in southern Tibet: insights from vorticity studies in Mabja Dome. Journal of Structural Geology 32, 70–85.

Larson, K.P., Godin, L., 2009. Kinematics of the Greater Himalayan series, Dhaulagiri Himal: implications for the structural framework of central Nepal. Journal of the Geological Society [London] 166, 25–43.

Law, R.D., 1990. Crystallographic fabrics: a selective review of their applications to research in structural geology. In: Knipe, R.J., Rutter, E.H. (Eds.), Deformation Mechanisms, Rheology and Tectonics. Geological Society, London, Special Publication, vol. 54, pp. 335–352.

Law, R.D., Morgan, S.S., Casey, M., Sylvester, C.M., Nyman, M., 1992. The Papoose Flat pluton of eastern California: a re-assessment of its emplacement history in the light of new microstructural and crystallographic fabric observations. Transactions of the Royal Society of Edinburgh: Earth Sciences 83, 361–375.

Law, R.D., Searle, M.P., Simpson, R.L., 2004. Strain, deformation temperatures and vorticity of flow at the top of the Greater Himalayan Slab, Everest Massif, Tibet. Journal of the Geological Society [London] 161, 305–320.
Lee, J., Dinklage, W.S., Hacker, B.R., Wang, Y., Gans, P.B., Calvert, A., Wan, J., Chen, W., Blythe, A., McClelland, W., 2000. Evolution of the Kangmar Dome, southern Tibet: structural, petrologic, and thermochronologic constraints. Tectonics 19, 872–896.
Lee, J., Dinklage, W.S., Wang, Y., Wan, J., 2002. Geology of the Kangmar Dome, southern Tibet with explanatory notes. In: Geological Society of America Map and Chart Series, MCH090, 1:50,000 scale, 8 p.
Lee, J., Hacker, B., Wang, Y., 2004. Evolution of North Himalayan gneiss domes: structural and metamorphic studies in Mabja Dome, southern Tibet. Journal of Structural Geology 26, 2297–2316.
Lee, J., McClelland, W., Wang, Y., Blythe, A., McWilliams, M., 2006. Oligocene-Miocene middle crustal flow in the southern Tibet: geochronology of Mabja Dome. In: Law, R.D., Searle, M.P., Godin, L. (Eds.), Channel Flow, Ductile Extrusion and Exhumation in Continental Collision Zones. Geological Society, London, Special Publication, vol. 268, pp. 445–469.
Lee, J., Whitehouse, M.J., 2007. Onset of mid-crustal extensional flow in southern Tibet: evidence from U/Pb zircon ages. Geology 35, 45–48.
Le Fort, P., 1975. Himalayas; the collided range; present knowledge of the continental arc. American Journal of Science 275-A, 1–44.
Leloup, P., Mahéo, G., Kali, E., Boutonnet, E., Liu, D., Xiahan, L., Haibing, L., 2010. The South Tibetan detachment shear zone in the Dinggye area: time constraints on extrusion models of the Himalayas. Earth and Planetary Science Letters 292, 1–16.
Lister, G.S., Dornsiepen, U.F., 1982. Fabric transitions in the Saxony granulite terrain. Journal of Structural Geology 4, 81–93.
Lister, G.S., Hobbs, B.E., 1980. The simulation of fabric development during plastic deformation and its application to quartzite: the influence of deformation history. Journal of Structural Geology 2, 355–370.
Lister, G.S., Paterson, M.S., Hobbs, B.E., 1978. The simulation of fabric development in plastic deformation and its application to quartzite: the model. Tectonophysics 45, 107–158.
Liu, G., Einsele, G., 1994. Sedimentary history of the Tethyan basin in the Tibetan Himalayas. Geologische Rundschau 82, 32–61.
Liu, Y., Siebel, W., Massonne, H., Xiao, X., 2007. Geochronological and petrological constraints for tectonic evolution of the central Greater Himalayan series in the Kharta area, southern Tibet. Journal of Geology 115, 215–242.
Lloyd, G.E., Freeman, B., 1994. Dynamic recrystallization of quartz under greenschist conditions. Journal of Structural Geology 16, 867–881.
Lombardo, B., Rolfo, F., 2000. Two contrasting eclogite types in the Himalayas: implications for the Himalayan orogeny. Journal of Geodynamics 30, 37–60.
Lombardo, B., Pertusati, P., Rolfo, F., Visonà, 1998. First report of eclogites from the E Himalaya: implications for the Himalayan orogeny. Memorie di Scienze Geogiche dell'Università di Padova 50, 67–68.
Mainprice, D., Bouchez, J.L., Blumenfeld, P., Tubia, J.M., 1986. Dominant c slip in naturally deformed quartz; implications for dramatic plastic softening at high temperature. Geology 14, 819–822.
Murphy, M.A., 2007. Isotopic characteristics of the Gurla Mandhata metamorphic core complex: implications for the architecture of the Himalayan orogen. Geology 35, 983–986.
Murphy, M.A., Copeland, P., 2005. Trantensional deformation in the central Himalaya and its role in accommodating growth of the Himalayan orogen. Tectonics 24, 1–19.
Murphy, M.A., Harrison, T.M., 1999. Relationship between leucogranites and the Qomolangma Detachment in the Rongbuk Valley, South Tibet. Geology 27, 831–834.
Murphy, M.A., Yin, A., Kapp, P., Harrison, T.M., Manning, C.E., 2002. Structural evolution of the Gurla Mandhata detachment system, southwest Tibet: implications for the eastward extent of the Karakoram fault system. Geological Society of America Bulletin 114, 428–447.
Nekvasil, H., Burnham, C.W., 1987. In: Mysen, B.O. (Ed.), The Calculated Individual Effects of Pressure and Water Content on Phase Equilibiria in the Granite System. Magmatic Processes: Physicochemical Principles. Geochemical Society, University Park, Pennsylvania, 500 p.
Nelson, K.D., Zhao, W., Brown, L.D., Kuo, J., Jinkai, C., Liu, X., Klemperer, S., Makovsky, Y., Meissner, R., Mechie, J., Kind, R., Wenzel, F., Ni, J., Nabelek, J., Leshou, C., Tan, H., Wei, W., Jones, A., Booker, J., Unsworth, M., Kidd, W., Hauck, M., Alsdorf, D., Ross, A., Cogan, M., Wu, C., Sandvol, E., Edwards, M., 1996. Partially molten middle crust beneath southern Tibet: synthesis of project INDEPTH results. Science 274, 1684–1688.
Nyman, M.W., Law, R.D., Morgan, S.S., 1995. Conditions of contact metamorphism, Papoose Flat Pluton, eastern California, USA: implications for cooling and strain histories. Journal of Metamorphic Geology 13, 627–643.
Okudaira, T., Takesbita, T., Hara, I., Ando, J., 1995. A new estimate of the conditions for transition from basal $\langle a \rangle$ to prism [c] slip in naturally deformed quartz. Tectonophysics 250, 31–46.
Passchier, C.W., 1987. Stable positions of rigid objects in non-coaxial flow: a study in vorticity analysis. Journal of Structural Geology 9, 679–690.
Passchier, C.W., 1988. The use of Mohr circles to describe non-coaxial progressive deformation. Tectonophysics 149, 323–338.
Passchier, C.W., Trouw, R.A.J., 2005. Microtectonics. Springer, Berlin, Heidelberg, New York.
Pognante, U., Benna, P., 1993. Metamorphic zonation, migmatization and leucogranites along the Everest transect of eastern Nepal and Tibet: record of an exhumation history. In: Geological Society, London, Special Publication, vol. 74, pp 323–340.
Pryer, L.L., 1993. Microstructures in feldspars from a major crustal thrust zone: the Grenville Front, Ontario, Canada. Journal of Structural Geology 15, 21–36.
Quigley, M., Liangjun, Y., Gregory, C., Corvino, A., Sandiford, M., Wilson, C.J.L., Xiaohan, L., 2008. U/Pb SHRIMP zircon geochronology and T-t-d history of the Kampa Dome, southern Tibet; implications for tectonic evolution of the North Himalayan gneiss domes. Tectonophysics 446, 97–113.
Quigley, M., Liangjun, Y., Xiaohan, L., Wilson, C.J.L., Sandiford, M., Phillips, D., 2006. $^{40}Ar/^{39}Ar$ thermochronology of the Kampa Dome, southern Tibet: implications for tectonics evolution of the North Himalayan gneiss domes. Tectonophysics 421, 269–297.
Simpson, R.L., Parrish, R.R., Searle, M.P., Waters, D.J., 2000. Two episodes of monazite crystallization during metamorphism and crustal melting in the Everest region of the Nepalese Himalaya. Geology 28, 403–406.
Simpson, C., Wintsch, R.P., 1989. Evidence for deformation-induced K-feldspar replacement by myrmekite. Journal of Metamorphic Geology 7, 261–275.
Searle, M., 1999. Extensional and compressional faults in the Everest–Lhotse massif, Khumbu Himalaya, Nepal. Journal of the Geological Society 156, 227–240.
Searle, M., Law, R., Jessup, M., 2006. Crustal structure, restoration and evolution of the Greater Himalaya in Nepal-South Tibet: implications for channel flow and ductile extrusion of the middle crust. In: Law, R.D., Searle, M.P., Godin, L. (Eds.), Channel Flow, Ductile Extrusion and Exhumation in Continental Collision Zones. Geological Society, London, Special Publication, vol. 268, pp. 355–378.
Searle, M., Law, R., Godin, L., Larson, K., Streule, M., Cottle, J., Jessup, M., 2008. Defining the Himalayan Central Thrust in Nepal. Journal of the Geological Society [London] 165, 523–534.
Searle, M.P., Simpson, R.L., Law, R.D., Parrish, R.R., Waters, D.J., 2003. The structural geometry, metamorphic and magmatic evolution of the Everest massif, High Himalaya of Nepal–South Tibet. Journal of the Geological Society [London] 160, 345–366.
Stipp, M., Stünitz, H., Heilbronner, R., Schmid, S.M., 2002a. The eastern Tonale fault zone: a 'natural laboratory' for crystal plastic deformation of quartz over a temperature range from 250 to 700 °C. Journal of Structural Geology 24, 1861–1884.
Stipp, M., Stünitz, H., Heilbronner, R., Schmid, S.M., 2002b. Dynamic recrystallization of quartz: correlation between natural and experimental conditions. In: De Meer, S., Drury, M.R., De Bresser, J.H.P., Pennock, G.M. (Eds.), Deformation Mechanisms, Rheology and Tectonics: Current Status and Future Perspectives. Geological Society, London, Special Publication, vol. 200, pp. 171–190.
Stockli, D.F., Taylor, M., Yin, A., Harrison, T.M., D'Andrea, J., Lin, D., Kapp, P., 2002. Late Miocene–Pliocene inception of E–W extension in Tibet as evidenced by apatite (U–Th)/He data. Geological Society of America Abstracts with Programs 34, 411.
Stormer, J.C., 1975. Practical two-feldspar geothermometer. American Mineralogist 60, 667–674.
Taylor, M., Yin, A., Ryerson, F., Kapp, P., Ding, L., 2003. Conjugate strike slip faulting along the Bangong–Nujiang suture zone accommodates coeval east-west extension and north–south shortening in the interior of the Tibetan Plateau. Tectonics 22, 1–16.
Theide, R.C., Arrowsmith, J.R., Bookhagen, B., 2005. From tectonically to erosionally controlled development of the Himalayan orogen. Geology 33, 689–692.
Theide, R.C., Arrowsmith, J.R., Bookhagen, B., McWilliams, M., Sobel, R., Strecker, M., 2006. Dome formation and extension in the Tethyan Himalaya, Leo Pargil, northwest India. Geological Society of America Bulletin 118, 635–650.
Tikoff, B., Fossen, H., 1995. The limitations of three-dimensional kinematic vorticity analysis. Journal of Structural Geology 17, 1771–1784.
Tullis, J., Christie, J.M., Griggs, D.T., 1973. Microstructures and preferred orientations of experimentally deformed quartzites. Geological Society of America Bulletin 84, 297–314.
Tullis, J., Yund, R., 1991. Diffusion creep in feldspar aggregates: experimental evidence. Journal of Structural Geology 13, 987–1000.
Tullis, J., Yund, R., 1992. The brittle-ductile transition in feldspar aggregates; an experimental study. In: Evans, B., Wong, T.F. (Eds.), Fault Mechanics and Transport Properties in Rocks. Academic Press, New York, pp. 89–118.
Vannay, J.-C., Grasemann, B., 1998. Inverted metamorphism in the High Himalaya of Himachal Pradesh (NW India): phase equilibria versus thermobarometry. Schweizerische Mineralogische und Petrographische Mitteilungen 78, 107–132.
Vernon, R.H., 1991. Questions about myrmekite in deformed rocks. Journal of Structural Geology 13, 979–985.
Viskupic, K., Hodges, K.V., Bowring, S.A., 2005. Timescales of melt generation and the thermal evolution of the Himalayan metamorphic core, Everest region, eastern Nepal. Contributions of Mineralogy and Petrology 149, 1–21.
Wallis, S.R., 1995. Vorticity analysis and recognition of ductile extension in the Sanbagawa belt, SW Japan. Journal of Structural Geology 17, 1077–1093.
Wallis, S.R., Platt, J.P., Knott, S.D., 1993. Recognition of syn-convergence extension in accretionary wedges with examples from the Calabrian Arc and the Eastern Alps. American Journal of Science 293, 463–495.
Wen, S., Nekvasil, H., 1994. SOLVCALC: an interactive graphics program package for calculating the ternary feldspar solvus and for two-feldspar geothermometry. Computers and Geosciences 20, 1025–1040.

Wenk, H.R., Canova, G., Molinari, A., Kocks, U.F., 1989. Viscoplastic modeling of texture development in quartzite. Journal of Geophysical Research 94, 17895–17906.
Whitney, J.A., Stormer, J.C., 1977. The distribution of $NaAlSi_3O_8$ between coexisting microcline and plagioclase and its effect on geothermometric calculations. American Mineralogist 62, 687–691.
Wu, C., Nelson, K.D., Wortman, G., Samson, S.D., Yue, Y., Li, J., Kidd, W.S.F., Edwards, M.A., 1998. Yadong cross structure and South Tibetan Detachment in the east central Himalaya (89°–90°E). Tectonics 17, 28–45.
Xypolias, P., 2009. Some new aspects of kinematic vorticity analysis in naturally deformed quartzites. Journal of Structural Geology 31, 3–10.
Xypolias, P., Koukouvelas, I.K., 2001. Kinematic vorticity and strain patterns associated with ductile extrusion in the Chelmos shear zone (External Hellenides, Greece). Tectonophysics 338, 59–77.
Zhang, J., Guo, L., 2007. Structure and geochronology of the southern Xainza-Dinggyê rift and its relationship to the South Tibetan detachment system. Journal of Asian Earth Sciences 29, 722–736.
Zhang, H., Harris, N., Parrish, R., Kelley, S., Zhang, L., Rogers, N., Argles, T., King, J., 2004. Causes and consequences of protracted melting of the mid-crust exposed in the North Himalayan antiform. Earth and Planetary Science Letters 228, 195–212.